LOW TEMPERATURE SPECIFIC HEAT STUDIES OF MOLYBDENUM-RUTHENIUM BASED SUPERCONDUCTING METALLIC GLASSES

Thesis by

Stuart Thomas Hopkins

In Partial Fulfillment of the Requirements

for the Degree of

Doctor of Philosophy

California Institute of Technology

Pasadena, California

1983

(Submitted September 20, 1982)

TO MY PARENTS

ACKNOWLEDGMENTS

I am very fortunate to have had the opportunity of working with Professor Bill Johnson. I feel that I have learned a great deal from Bill, and I wish to express my appreciation for his patience, understanding, and guidance. It has been a pleasure to know the wisdom and humour of Professor Pol Duwez. I am grateful to Bill, to Professor, and to all the members of our group for providing such a pleasant and memorable place to work.

I would like to thank Albert Highe, Andy Hunter, Art Williams, Bruce Clemens, Gord Mitchard, Randy Feenstra and Reuben Collins for many helpful and stimulating discussions. I owe special thanks to Tom Cardell, who has always supported and encouraged my education. I also wish to thank Professor Tom McGill for his help and advice, and Dr. Roderick Turner for his warm hospitality.

For their excellent technical assistance and many helpful suggestions, I wish to thank Angela Bressan, Concetto Geremia, Elmer Szombathy and George Griffith. The work of Sumio Kotake and Dr. Robert Shull in the initial stages of the specific heat project was invaluable.

Finally, I would like to thank Jennifer Loeppky for her care and patience in typing the thesis.

Financial support from the Natural Sciences and Engineering Research Council of Canada and the United States Department of Energy is gratefully acknowledged.

ABSTRACT

Low temperature specific heat measurements have been used to investigate the electronic structure and superconducting properties of metallic glasses based on transition metals Mo and Ru alloyed with metalloids B and Si. An apparatus constructed for making these measurements is described. The results obtained are discussed in terms of the dependence of the density of states at the Fermi level $N(\varepsilon_F)$ and of the Debye temperature θ_D on metalloid content, and the influence of these parameters on observed properties. $N(\varepsilon_F)$ is shown to reflect the short-range order of the metal atoms and in Mo-Ru-B alloys, indicates the existence of two distinct amorphous phases. In addition, $N(\varepsilon_F)$ strongly influences the superconductivity and electronic properties of these materials. Alloying with metalloids increases the Debye temperature of the amorphous Mo-Ru phase and thus affects the superconductivity through the dependence of the electron-phonon coupling on average phonon frequency. A comparison with elastic properties shows an anomalous effect in the lattice specific heat commonly observed in insulating glasses.

TABLE OF CONTENTS

LIST OF TABLES

LIST OF FIGURES

I. INTRODUCTION

I. INTRODUCTION

The primary objective of this study is to obtain the low temperature specific heat of two series of transition metal-metalloid glasses based on molybdenum and ruthenium. To do so, we have constructed apparatus for use with a thermal relaxation method which allows the heat capacities of very small samples to be determined. The results of these measurements allow us to examine the composition dependence of the density of states at the Fermi level and of the Debye temperature in these alloys. We thus obtain structural information which gives insight into the electronic and superconducting properties of the material. Conversely, analysis of the superconductivity reveals a great deal about the structure. The behaviour of these alloys is considered in the context of two more general problems: the electronic structure of transition metal-metalloid metallic glasses and in particular the role of the metalloids; and the systematics of superconductivity in transition metals and alloys.

A fundamental problem in solid state physics lies in understanding the electronic structure and properties of metals. Until recently, most emphasis was placed on crystalline metals, in which the atomic structure can be defined in terms of the positions of a very small fraction of the total number of atoms. The impetus for studying non-crystalline bulk metals came with the work of Duwez [1], who demonstrated that stable non-crystalline alloys could be obtained in bulk

form by rapid quenching. However, in amorphous systems, the long-range symmetry which characterizes crystalline solids is absent. Consequently, a description of the structure of an amorphous solid in terms of the positions of all the atoms is not possible. The question of the electronic structure of amorphous metals is further complicated by the lack of a well defined band structure $\varepsilon(\vec{k})$. This follows from the non-periodicity of the lattice, since $\vec{k}$ is no longer conserved.

A concept which is highly useful for describing electronic structure and which is applicable to both crystalline and non-crystalline metals is the density of electron states $N(\varepsilon)$, particularly the density of states at the Fermi level $N(\varepsilon_F)$. In d-band metals, the behaviour of $N(\varepsilon_F)$ largely determines the transport properties, and is a very sensitive probe of the local environment of the transition metal atoms [2]. The most direct experimental measure of $N(\varepsilon_F)$ is provided by low temperature specific heat measurements. The specific heat of a normal metal at low temperatures can often be described by $C = \gamma T + \beta T^3$ where the electronic coefficient γ is proportional to $N(\varepsilon_F)$. In addition, the Debye temperature θ_D which characterizes the phonon system can be extracted from the coefficient β. Hence, specific heat measurements give direct information about microscopic parameters influencing properties such as transport and superconductivity.

In studying metallic glasses, one must frequently overcome experimental difficulties associated with having materials

only available in small quantities. One such case is in the measurement of heat capacity, since traditional adiabatic techniques require relatively large samples. Since techniques for measuring small-sample heat capacities have only been developed recently, the use of low temperature calorimetry in metallic glass research is relatively new. However, such experiments have already yielded information obtainable from no other experimental technique, and promise to contribute a great deal to our understanding of the fundamental nature of the structure of metallic glasses.

II. THEORY AND BACKGROUND

II.1 SPECIFIC HEAT

A. Thermodynamics

Measurements of specific heat have long been important in studying all states of matter. As early as 1819, Dulong and Petit had formulated an empirical rule describing the specific heat of solids, which was subsequently accounted for by classical equipartition theory [3]. It was later realized that quantum effects were clearly manifested in the specific heat of solids at low temperatures. The models of Einstein and Debye, which view atoms in solids as quantum mechanical oscillators, accounted for the observed breakdown of the Dulong-Petit law at low temperatures.

The usefulness of specific heat as an experimental tool lies in its direct connection with fundamental thermodynamic quantities such as entropy. In addition, a theoretical description of a system in terms of energy levels allows a partition function to be defined, from which the specific heat can be directly computed.

The specific heat is defined by [4]

$$C_\alpha = \left(\frac{dQ}{dT}\right)_\alpha$$

where an amount of heat dQ raises the temperature of a unit mass of a substance by an amount dT while a given property α is held fixed. In principle, the parameter α could represent a large number of physical properties of a given system. Practically though, only the specific heats at constant pressure and volume, C_P and C_V, are important. The difference

between the two is expressible in terms of the thermal expansion coefficient $\alpha = V^{-1}(\partial V/\partial T)_P$ and the isothermal compressibility k_T as

$$C_P - C_V = \frac{TV\alpha^2}{k_T} \qquad (1)$$

where V is the molar volume.

C_V can be calculated directly from the internal energy; since

$$dE = TdS - PdV \quad ,$$

C_V is given by

$$C_V = T\left(\frac{\partial S}{\partial T}\right)_V = \left(\frac{\partial E}{\partial T}\right)_V \qquad (2)$$

According to the third law of thermodynamics, the entropy of a system in thermal equilibrium must approach zero at a temperature of absolute zero. Hence, integrating (2),

$$S(T') = \int_0^{T'} \frac{C_V}{T}\, dT$$

where S(T') is the entropy at a temperature T'. This is a very useful fact, since if specific heat data can be taken to sufficiently low temperature and extrapolated to zero, the entropy of the system can be calculated.

Statistical methods are generally used to reveal the detailed thermal behaviour of a system. These yield descriptions in terms of a set of energy levels ε_j which can be occupied by the particles or excitations of the system. The partition function of the system, given by

$$Z = \sum_j \exp\left(-\frac{\varepsilon_j}{k_B T}\right)$$

can then be calculated and used to obtain the Helmholtz free energy, $F = -k_B T \ln Z$, and the specific heat

$$C_V = -T\left(\frac{\partial^2 F}{\partial T^2}\right)_V \quad .$$

It is evident that calculations generally yield values for the specific heat at constant volume. For solids, however, measurements of specific heat are normally made at constant pressure owing to the experimental difficulties involved in making constant volume measurements. Thus, C_V is usually obtained by measuring C_p and using equation (1) or a suitable approximation [3]. Fortunately, at low temperatures, C_p and C_V differ negligibly and such corrections are not necessary. This can be seen in the behaviour of the expansion coefficient α which vanishes with roughly the same temperature dependence as the specific heat. Hence, the right hand side of equation (1) is vanishingly small at low temperatures.

B. Low Temperature Specific Heat of Normal Metals

The specific heat of a normal metal at low temperatures (neglecting nuclear quadrupole interactions, magnetic effects, etc.) is well represented by a series in odd powers of temperature

$$C = \sum_{n=1,3,5\ldots} A_n T^n$$

where the linear (n=1) term is due to the heat capacity of conduction electrons and higher order terms arise primarily from the lattice heat capacity. For most metals, the first two terms suffice to describe the heat capacity to an accuracy of better than 1% at temperatures in the liquid helium range. Hence, the low temperature specific heat of metals is usually written as

$$C_V = \gamma T + \beta T^3 \quad .$$

In this section, we discuss the physical basis of models used to interpret the coefficients γ and β.

Formally, the problem of lattice specific heat can be approached as follows. For small oscillations, the harmonic approximation can be applied to the thermal vibrations of an assembly of N ions. This allows the collective vibrations of the ions to be resolved into a set of 3N noninteracting harmonic oscillators; i.e., the normal modes. The partition function can then be expressed as the product of the individual partition functions of the 3N normal modes,

$$Z = \prod_{\alpha}^{3N} Z_\alpha \quad .$$

The functions Z_α are given by

$$Z_\alpha = \sum_{j=0}^{\infty} \exp\left(-\frac{(j+\tfrac{1}{2})\hbar\omega_\alpha}{k_B T}\right)$$

where $\varepsilon_j = (j+\tfrac{1}{2})\hbar\omega_\alpha$ is the quantized energy of the jth level. The free energy of the system is

$$F = F_o + k_B T \sum_\alpha \ln\left(1 - e^{-\hbar\omega_\alpha / k_B T}\right)$$

where F_o is a constant related to the zero point energy of the solid. It is convenient to define a vibrational frequency distribution $g(\omega)$, whereby $g(\omega)d\omega$ = the number of modes with frequency in the interval $(\omega, \omega + d\omega)$. (An integral over all frequencies gives the total number of modes $\int_o^\infty g(\omega)d\omega = 3N$). The free energy can then be expressed in terms of an integral over the normal mode frequencies,

$$F = F_o + k_B T \int_0^\infty \ln\left(1 - e^{-\hbar\omega / k_B T}\right) g(\omega)d\omega$$

and the specific heat at constant volume is

$$C_V = k_B \int_0^\infty \frac{(\hbar\omega/k_B T)^2 \, e^{\hbar\omega/k_B T}}{\left(e^{\hbar\omega/k_B T} - 1\right)^2} g(\omega)d\omega \qquad (3)$$

Thus, the lattice specific heat is dictated by details of the normal mode distribution $g(\omega)$.

It was first shown by Einstein in 1907 that the quantization of vibrational energy in a solid leads to a reduction in the specific heat at low temperatures. In the simple Einstein model, all ions vibrate at the same characteristic frequency ω_E. With $g_E(\omega) = 3N\delta(\omega - \omega_E)$ substituted into equation (3), we find that at low temperatures $C_V \sim (1/T^2) \exp(-\hbar\omega_E/k_B T)$. Although this is not the correct temperature dependence, the Einstein model is still useful as a model for optical phonons. At low temperatures, only low frequency, long wavelength modes are excited, and details of

the atomic arrangements are unimportant. This is the basis of the well-known Debye model, which views lattice vibrations as the acoustic oscillations of an elastic continuum. In this model, the normal mode frequency distribution is quadratic out to a maximum frequency ω_D:

$$g_D(\omega) = \begin{cases} \frac{3V}{2\pi^2 C_S^3}\,\omega^2 & \omega \leq \omega_D \\ 0 & \omega \geq \omega_D \end{cases}$$

where C_S is an effective sound velocity. This distribution follows from the linear dispersion relation of sound waves. The cutoff frequency ω_D, known as the Debye frequency, depends only on the sound velocities in the solid and on the number of atoms in the solid. With $g_D(\omega)$ substituted into (3), in the limit of low temperatures we obtain

$$C_V \to \frac{12\pi^4}{5} Nk_B \left(\frac{T}{\theta_D}\right)^3 \equiv \beta T^3$$

where the Debye temperature θ_D is defined as $h\omega_D/k_B$. For an isotropic solid, the sound velocity C_S is a weighted average of longitudinal and transverse sound velocities, whereby $3/C_S^3 = 2/C_T^3 + 1/C_L^3$. Since C_L and C_T can be defined in terms of the elastic moduli, the Debye temperature can be calculated from measured sound velocities or elastic moduli. For example, θ_D can be written in terms of Young's modulus E and the density ρ as

$$\theta_D = \frac{\hbar}{k_B} f(\nu)\left(\frac{E}{\rho}\right)^{1/2}\left(\frac{N}{V}\right)^{1/3}$$

where $f(\nu)$ is a dimensionless function of Poisson's ratio ν.

Although the Debye model correctly predicts the temperature dependence of the specific heat at low temperatures, deviations from the Debye form of $g(\omega)$ in a real solid are considerable. In actuality, the normal mode dispersion relations are not linear. A more realistic distribution includes higher order terms

$$g(\omega) = \alpha_2\omega^2 + \alpha_4\omega^4 + \alpha_6\omega^6 + \ldots$$

giving higher terms in the specific heat [5]

$$C = \beta T^3 + \delta T^5 + \alpha T^7 + \ldots \quad .$$

Terms higher than n=3 become increasingly important for temperatures greater than about $\theta_D/30$. The lack of odd order terms in the frequency distribution is a consequence of the symmetry of interatomic forces [6].

According to classical equipartition theory, which is reasonably successful in describing the transport of conduction electrons in metals, the specific heat of the electrons should be comparable to that of the ions in the lattice. In fact, the electronic specific heat is considerably lower than predicted and at room temperature is completely masked by the lattice specific heat. Although the internal energy of the electron gas is very large, it changes little with temperature. This is a consequence of Fermi-Dirac statistics which are obeyed by the electrons. At a temperature T, only a small fraction of the electrons, on the order of k_BT/ε_F is thermally excited with each electron acquiring an energy $\sim k_BT$. Since

the Fermi energy ε_F is on the order of 10^5K for most metals, the electronic specific heat is $\sim Nk_B(k_BT/\varepsilon_F)$ which is approximately .01 Nk_B at room temperature. The lattice specific heat, by comparison, is $\sim Nk_B$. However, at low temperature, where the lattice specific heat vanishes as T^3, the linearly temperature-dependent electronic specific heat becomes observable.

The electronic specific heat can be calculated in detail by evaluating the integral describing the mean energy of the electron gas,

$$E = 2\int_0^\infty \varepsilon f(\varepsilon) N(\varepsilon)\, d\varepsilon$$

where $f(\varepsilon)$ is the Fermi function $(e^{(\varepsilon-\mu)/k_BT} + 1)^{-1}$ and $N(\varepsilon)$ is the single spin density of electron states. Integrals of this type are evaluated by exploiting the fact that the derivative of $f(\varepsilon)$ is zero everywhere except in a narrow region of width $\sim k_BT$ near $\varepsilon=\mu$. This leads to a series expansion of E in terms of k_BT which, to second order in k_BT, is

$$E = E_o + \frac{\pi^2}{3}(k_BT)^2 N(\varepsilon_F)$$

giving

$$C_V = \frac{2\pi^2}{3} k_B^2 N(\varepsilon_F) T \equiv \gamma T$$

In the free-electron model,

$$\gamma = \frac{\pi^2}{2} k_B^2 \frac{n}{\varepsilon_F}$$

and is only a function of the electron density n. Reasonable agreement with experiment is obtained for monovalent metals

such as the alkali series and to a lesser extent for the noble metals. Discrepancies are commonly expressed in terms of a thermal effective mass ratio $m^*/m = \gamma_{measured}/\gamma_{free\ electron}$. Very high values of m^*/m are obtained for transition metals, indicating large departures from the free electron description. There are two main reasons for this: large densities of states near the Fermi level due to the d-bands of the metal, and enhancement of the electron mass due to interaction with phonons. The first factor is illustrated in Fig. 1. In this simple picture of the band structure of a transition metal (neglecting hybridization), the bands are divided into very broad s-bands and relatively flat d-bands. The former describe the nearly-free s-like conduction electrons, while the d-bands correspond to the highly localized d electrons. This results in a density of states like that shown in the figure. One or two s electrons in states spread over approximately 10 eV make a small contribution to the density of states, while up to 10 d electrons are accommodated by states in a range of about 5 eV resulting in a very large d-band contribution to $N(\varepsilon)$. Since the d-bands are not completely full, the Fermi level lies in the region of the d states, where the density is largest. In crystalline metals, the Fermi level frequently lies on a singularity in the density of states arising from regions of the d-band structure where $d\varepsilon/dk$ goes to zero. Consequently, the value of γ is very large in these materials. Examples among the 4d transition elements are Y, Nb, and Pd which have γ values on the order of ten times typical free-electron

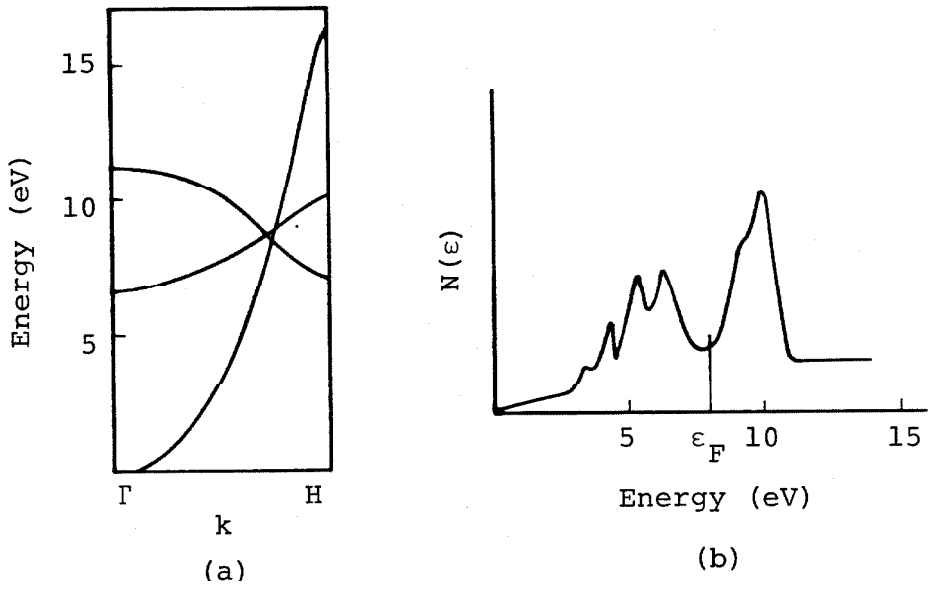

Figure 1. Simplified illustration of (a) energy bands, and (b) density of states, for a bcc transition metal. In (a), k is shown for the (100) direction. The position of the Fermi energy in (b) is appropriate for Cr or Mo. (After reference 8 (b).)

values [7]. Although increased scattering in amorphous materials leads to a smearing of sharp structure in $N(\epsilon)$, these essential features remain: a large contribution to $N(\epsilon_F)$ due to d electrons, and correspondingly high values of γ.

For electrons near the Fermi surface (on the scale of phonon energies), interactions with phonons shifts the electronic energies by a factor $1/(1 + \lambda)$. These energy shifts result from screening of the electron-electron Coulomb interaction by the ions [8]. Physically, this can be thought of as the effect of the electron carrying along a "wake" of phonons. As a consequence, the electronic velocity is decreased and the density of levels at the Fermi surface is enhanced by a factor of $(1 + \lambda)$, whereby

$$\gamma = \frac{2}{3} \pi^2 k_B^2 N(\epsilon_F)(1 + \lambda) \quad .$$

In this expression, $N(\epsilon_F)$ again refers to the density of states for one spin orientation.

II.2 SUPERCONDUCTIVITY

A. Electronic Specific Heat of Superconductors

One of the distinguishing features of the superconducting state is the expulsion of magnetic flux from the interior of a superconductor. Application of a magnetic field greater than a value known as the thermodynamic critical field H_C destroys this perfect diamagnetism. H_C depends on temperature and at a temperature T, the free energy difference between the normal

and superconducting states, known as the condensation energy, is given by [9]

$$f_n(T) - f_S(T) = \frac{H_C^2(T)}{8\pi} \quad .$$

(f_n and f_S represent the zero field Helmholtz free energies per unit volume of the normal and superconducting states respectively.) It follows that the entropy difference is

$$S_n - S_S = - \frac{H_C}{4\pi} \frac{\partial H_C}{\partial T} \quad .$$

At the critical temperature T_C, where the thermodynamic critical field vanishes, the zero field entropies are equal. However, the corresponding specific heats are not equal at T_C:

$$(C_n - C_S)\Big|_{T_C} = T \frac{\partial}{\partial T} (S_n - S_S)\Big|_{T_C}$$

$$= - \frac{T_C}{4\pi} \left(\frac{\partial H_C}{\partial T} \right)^2$$

Hence, the electronic specific heat is discontinuous at T_C as shown in Fig. 2.

The manner in which a magnetic field penetrates a superconductor leads to a division into two types [10]. Superconductors known as type II exhibit properties which are described in terms of temperature dependent critical fields H_{C_1} and H_{C_2}. Roughly speaking, if a field less than H_{C_1} is applied to a type II superconductor, the field is expelled. For fields intermediate between H_{C_1} and H_{C_2}, the flux penetrates the sample

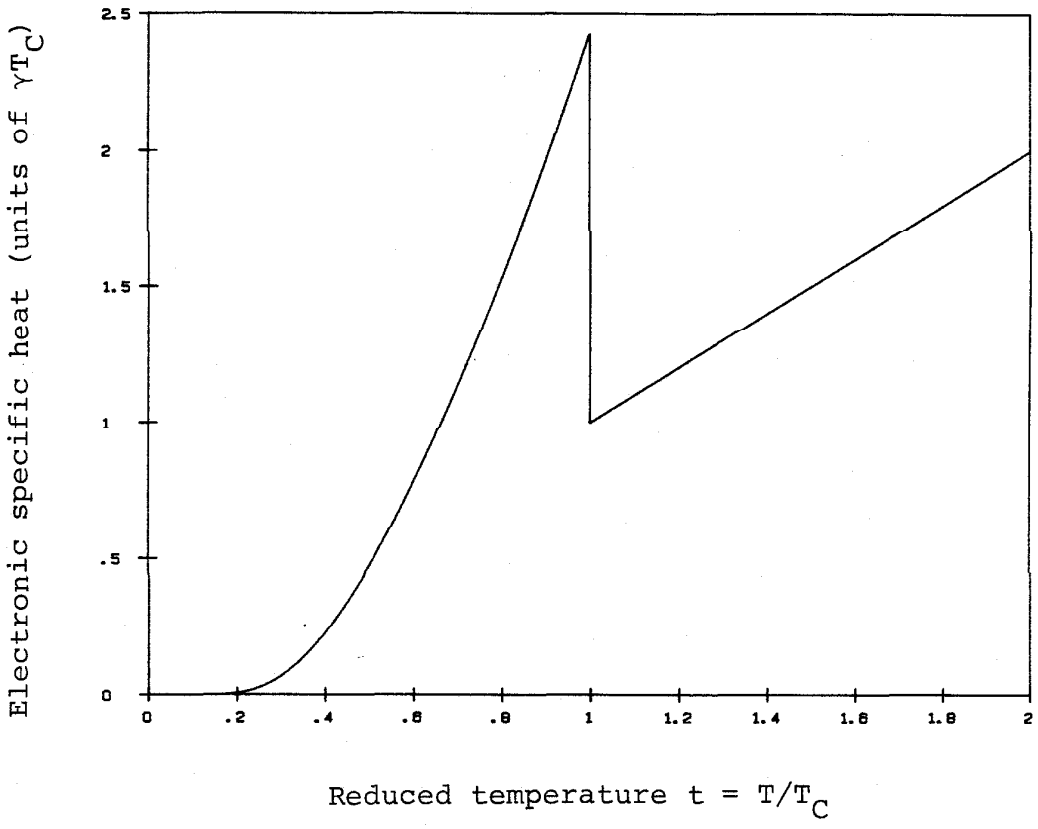

Figure 2. Electronic specific heat in reduced units predicted by BCS theory.

forming the "mixed" state in which the flux exists in quantized bundles enclosed by supercurrent vortices. For fields greater than the upper critical field H_{C_2}, flux completely penetrates the sample and it is no longer superconducting. The value of the thermodynamic critical field H_C defined above lies between H_{C_1} and H_{C_2} so for type II materials, it is not an actual "critical" field.

Although the thermodynamic relations agree well with experiment, no insight is given into the microscopic nature of superconductivity. First elucidated in the theory of Bardeen, Cooper and Schrieffer [11], superconductivity involves a pairing of electrons due to an attractive electron-phonon coupling. A certain energy is required to break a pair and this produces an energy gap in the excitation spectrum of the quasiparticles created from the paired electrons. The presence of an energy gap drastically alters the electronic specific heat in the superconducting state. It gives rise to the effects predicted by thermodynamics, such as the discontinuity at T_C. In the BCS picture of superconductivity, fermion quasiparticles are thermally excited to states above the gap with energy given by [9]

$$E = \sqrt{\xi^2 + \Delta(T)^2} \tag{4}$$

where $\Delta(T)$ is the temperature dependent gap energy and ξ are single particle energies referred to the Fermi level. From considering the entropy of a fermion gas with excitation spectrum given by (4), the specific heat is obtained as [12]

$$C_S = -\frac{2}{T} N(\varepsilon_F) \int_{-\infty}^{+\infty} d\varepsilon \left(E^2 + \frac{\beta}{2} \frac{\partial \Delta^2}{\partial \beta} \right) \frac{\partial f}{\partial E}$$

where $\beta \equiv 1/k_B T$ and f is the Fermi function. The first term in the integrand represents the specific heat of the quasiparticles in the various energy states E, while the second term arises from the rearrangement of the energy states due to the temperature dependence of the gap. Using this expression, the magnitude of the discontinuity in the electronic specific heat can be calculated. One obtains

$$\left. \frac{C_S - C_n}{C_n} \right|_{T_C} = 1.43 \quad .$$

It is customary to model the specific heat by $e^{-\Delta(T)/k_B T}$ to extract a value for the zero temperature gap energy and even the temperature dependence of the gap. Strictly speaking, the specific heat does not show this dependence, even for so-called BCS superconductors [13]. The presence of the gap will produce a dominant term in the specific heat of the form $Ae^{-B/T}$ but in general, the coefficient B is not related in a simple way to the gap energy of the BCS theory at all temperatures below T_C. In the original treatment, the expression given for the specific heat at $T << T_C$ is [11]

$$\frac{C_S}{\gamma T_C} = \frac{3}{2\pi^2} \left(\frac{\Delta(0)}{k_B T_C} \right) \left(\frac{T_C}{T} \right)^2 \left[3K_1 \left(\frac{\Delta(0)}{k_B T} \right) + K_3 \left(\frac{\Delta(0)}{k_B T} \right) \right]$$

where K_n are modified Bessel functions of the second kind.

Using the asymptotic form of the Bessel functions [14], this reduces to

$$\frac{C_S}{\gamma T_C} \simeq 3.09 \left(\frac{T_C}{T}\right)^{3/2} e^{-1.75T_C/T}$$

but this is only valid for $T \sim T_C/100$. A useful expression, also given in the original paper although not in the correct limit, is [11]

$$C_S \simeq 8.5\ \gamma T_C\ e^{-1.44T_C/T} \quad . \tag{5}$$

As shown in Fig. 3, this closely approximates the exact BCS result, as computed by Mühlschlegel [13], in the temperature range $0.2\ T_C < T < 0.6\ T_C$. The expression in equation (5) can be used to compare predictions of the BCS theory with specific heat data measured in this temperature range and fitted to the form $Ae^{-B/T}$.

B. Results of Strong-Coupling Theory

In this section, we discuss facts about strong-coupling theories of superconductivity relevant to the analysis of specific heat data. The BCS theory applies to materials in which the electron-phonon coupling is weak, i.e., $\lambda << 1$. Microscopic parameters responsible for superconductivity enter the BCS theory in a simple way. In the BCS theory, the transition temperature is related to the coupling constant λ and a characteristic phonon frequency $\langle\omega\rangle$ through the relation [12]

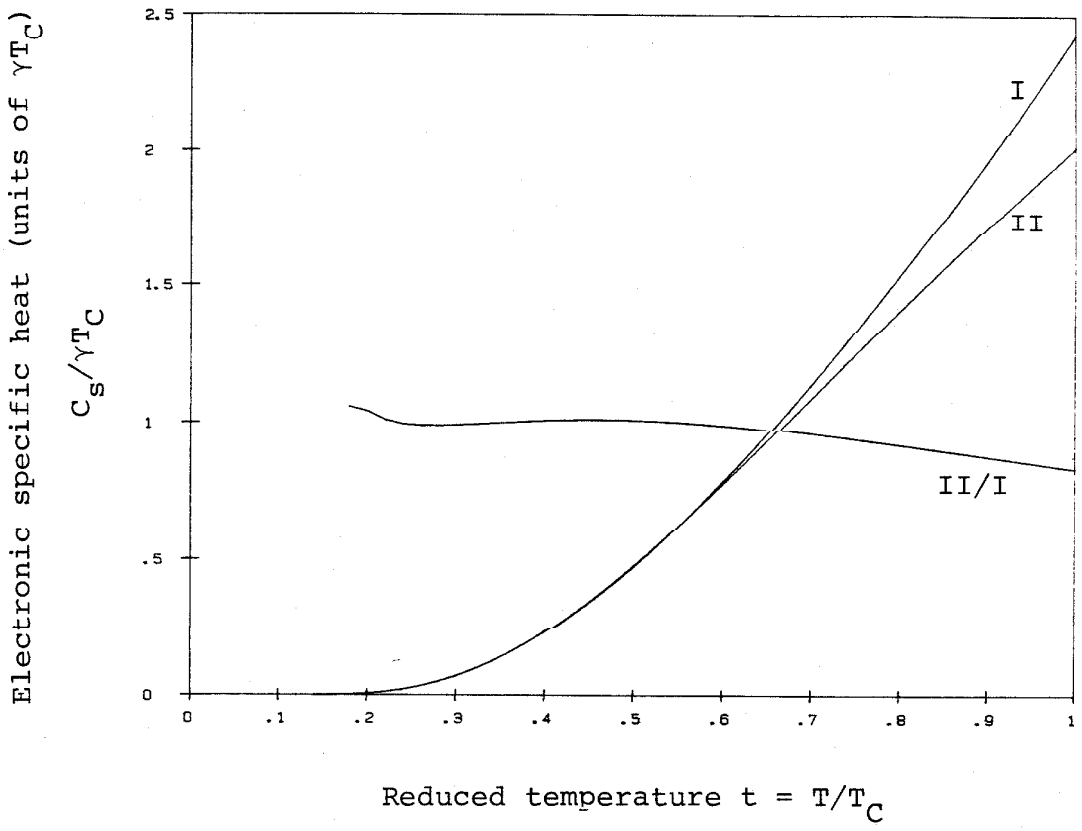

Figure 3. Comparison of exact solution of BCS equations for electronic specific heat in the superconducting state (I), and approximate form $8.5e^{-1.44/t}$ (II). Note agreement in the range $0.2 \leq t \leq 0.6$.

$$T_C = 1.13 \langle\omega\rangle e^{-1/\lambda} \quad .$$

The coupling constant is given by the product of the density of states at the Fermi level $N(\varepsilon_F)$ and an effective electron-phonon matrix element V. Attempts to verify this equation using values of T_C, θ_D, and $N(\varepsilon_F)$ determined from specific heat measurements meet with little success, since V depends on $N(\varepsilon_F)$ and $\langle\omega\rangle$ in a nontrivial way.

The relation between microscopic parameters and observed transition temperature was first studied extensively by McMillan [15]. Based on the Eliashberg theory of superconductivity [16], a central result of McMillan's work is an expression relating T_C to the coupling constant λ and averaged phonon frequency $\langle\omega\rangle$:

$$T_C = \frac{\langle\omega\rangle}{1.20} \exp\left[-\frac{1.04(1+\lambda)}{\lambda - \mu^*(1+0.62\lambda)}\right]$$

where μ^* is the Coulomb pseudopotential describing the repulsive Coulomb interaction between two electrons. λ can be defined in terms of the electron-phonon spectral function $\alpha^2F(\omega)$ as

$$\lambda = 2\int d\omega\alpha^2 F(\omega)/\omega$$

where $F(\omega)$ represents the phonon density of states and $\alpha^2(\omega)$ is an averaged frequency-dependent electron-phonon matrix element. Thus, the McMillan theory is based on a much more realistic view of the material parameters than is the BCS theory. The prefactor in the McMillan expression appears in

many forms in the literature. Usually it involves $\langle\omega\rangle$ or $\langle\omega^2\rangle^{\frac{1}{2}}$, where

$$\langle\omega^n\rangle = \frac{2}{\lambda}\int d\omega\alpha^2 F(\omega) \omega^{n-1} \quad .$$

Experimentally, the function $\alpha^2F(\omega)$ is obtainable from superconducting tunnelling measurements, but a more common procedure is to use the Debye temperature to approximate the characteristic phonon frequency, even though this is sometimes not a good representation of $\langle\omega\rangle$.

Allen and Dynes [17] later showed that the McMillan equation is applicable to a wide variety of intermediate-coupled materials, i.e., those for which $0.5 < \lambda < 1$. However, for $\lambda > 1$, a more complicated logarithmically averaged prefactor must be used. The McMillan equation is thus widely used to estimate the magnitude of the coupling constant from specific heat data. For transition metals, a value of $\mu^* = 0.13$ is used [15].

McMillan also showed that λ can be written in terms of electronic matrix elements and phonon frequencies as

$$\lambda = \frac{N(\varepsilon_F)\langle I^2\rangle}{M\langle\omega^2\rangle}$$

where M is the ionic mass, and $\langle I^2\rangle$ is a Fermi surface averaged squared electronic matrix element.

Another result from the theory of strong-coupled superconductors which is used in analyzing specific heat data concerns the relationship between the normal state electronic

specific heat coefficient γ, and the slope of the upper critical field at the transition temperature, $dH_{c_2}/dT\big|_{T_c}$. For superconductors in which the mean free path of the electrons is much less than the coherence length, it is predicted that [18]

$$\gamma = - \frac{1}{4.48 \times 10^4 \rho} \left. \frac{dH_{c_2}}{dT} \right|_{T_c}$$

where ρ is the normal state resistivity in ohm cm, γ is in ergs cm^{-3} K^{-2} and the gradient is given in Oe K^{-1}.

II.3 METALLIC GLASSES

The term metallic glass is generally applied to non-crystalline, metastable alloys prepared by rapid cooling from the liquid state. The strategy used in forming metallic glasses is to cool the liquid sufficiently quickly to avoid crystallization and thereby preserve the structure of the liquid. To do so requires cooling the liquid below the glass transition temperature T_g which lies below the melting point [19,20]. Although the material is amorphous above and below the glass transition, a fundamental change occurs there. Above T_g, the time required for atomic rearrangements is very short and atomic motions are largely translational. At T_g, the time associated with atomic translation becomes extremely long (typically on the order of 1 day) and below this point atomic motion is confined to vibrations about

equilibrium positions in a fixed lattice. (For the moment, we neglect structural relaxation processes.) The change at T_g is reflected in viscosity, which increases by several orders of magnitude over a few degrees of temperature near T_g, and specific heat, which decreases rapidly and approaches the specific heat of the corresponding crystalline phase. Thermodynamically, the supercooled liquid, which is in metastable equilibrium above T_g, makes a transition to the glass state. The drop in specific heat is a result of equilibrium configurations of the liquid becoming inaccessible as the complex atomic motions of the liquid are frozen out. The glass is thus frozen into a restricted region of configuration space, which can be thought of as a local free energy minimum. It has been well established that the principles of thermodynamics apply in this region of configuration space, on the time scale of most thermal measurements [3,19].

Upon heating, atomic rearrangements occur and the glass can move to other regions of configuration space. Given sufficient thermal energy, the system will eventually find the free energy minimum corresponding to its equilibrium crystalline state. This normally occurs at a fairly well defined temperature near T_g although this is strongly dependent on the heating rate. Annealing below the crystallization temperature can bring about structural relaxation processes involving changes in free volume; such processes are not necessarily related to crystallization.

The "freezing" of liquid alloys into glasses can be accomplished by rapid quenching if the growth of crystalline

nuclei is given insufficient time to occur. The two most widely used methods of rapid quenching are the piston and anvil [21], or splat-quenching technique, and the melt-spinning technique [22]. In the piston and anvil technique, a molten droplet of the alloy is cooled between the parallel faces of a fast-moving piston and a fixed anvil. Samples prepared in this manner are in the form of round foils, typically 1-2 cm. in diameter and on the order of 50 μm in thickness. A more important method commercially is the melt-spinning technique which allows large amounts of material to be prepared. In this method, a stream of the molten alloys flows under pressure onto the surface of a rapidly spinning copper or steel wheel. The liquid quickly cools and spins off as a ribbon of metallic glass. In this way, material in many forms, from fibers to sheets several inches in widths, can be fabricated. Both of these methods achieve cooling rates on the order of 10^5 to 10^6 degrees per second, which is high enough to allow a wide variety of metallic glass alloys to be prepared.

By far the largest group of metallic glasses are the transition metal-metalloid glasses. These alloys have composition $TM_{1-x}M_x$ where TM represents transition metal atoms and M represents metalloid or "glass-former" atoms such as B, P, Si, and C. The metalloid content x is generally around 20%, but for most of these alloys, a range of x exists over which the alloys can be made amorphous. The glass-forming range is very often close to a eutectic composition, nominally

$TM_{80}M_{20}$. Glass formation is favored there since the liquidus temperature is closest to the glass transition temperature in this region of the phase diagram [19].

The main source of structural information on metallic glasses is obtained from X-ray diffraction studies. Diffraction patterns can readily reveal whether a material is crystalline or amorphous. The diffraction pattern of a crystalline material exhibits a series of sharp peaks. These are the diffraction maxima, corresponding to the well-defined atomic spacings in the crystal. In non-crystalline materials, this is not the case and the pattern consists of a small number of very broad bands. In addition to being useful for qualitative characterization, diffraction measurements provide quantitative information in the form of radial distribution functions. These are related by a Fourier transform to the diffraction intensity patterns. Figure 4 shows the reduced radial distribution function $G(r) = 4\pi r(\rho(r) - \rho_o)$ for a $(W_{0.5}Ru_{0.5})_{80}B_{20}$ alloy [23]. In this expression, $\rho(r)$ is the atomic density at a distance r from a given atom and ρ_o is the mean density. At a distance of about five atomic diameters, the atomic positions are no longer correlated and the density $\rho(r)$ approaches the mean density ρ_o. Hence, the function G(r) approaches zero. Herein lies a distinguishing feature of the amorphous state--the lack of long-range correlations in atomic positions, i.e., long-range order. At distances closer to r=0, the function exhibits a series of peaks corresponding to successive atomic shells around the

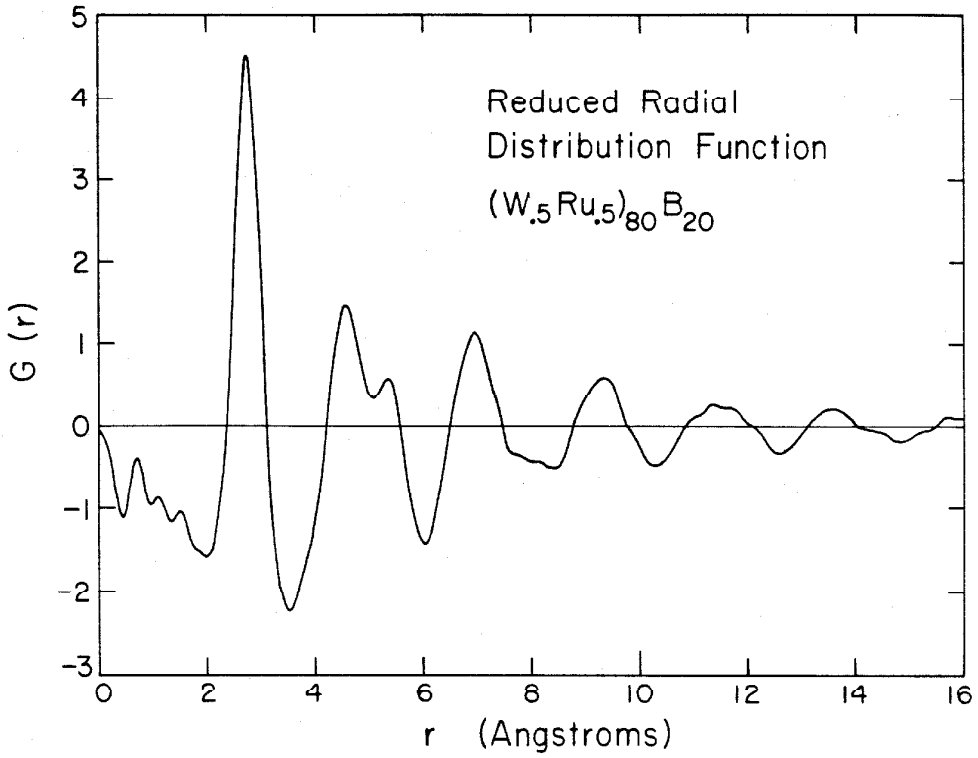

Figure 4. Reduced radial distribution function $G(r) = 4\pi r(\rho(r) - \rho_o)$ for amorphous $(W_{.5}Ru_{.5})_{80}B_{20}$. (Taken from reference 23.)

given atom. The position of the first peak is well defined and gives the most probable nearest-neighbor separation. The area under this peak is related to the coordination number of the metal atoms. Coordination numbers for metal atoms in TM-M glasses are usually around 12, which is comparable to the number of nearest neighbors that an atom has in a close-packed crystal. It should be emphasized that the radial distribution function does not represent a unique characterization of the structure since it involves a radial average of atomic positions. However, it does serve as a check on structural models. Models based on dense random packings agree well with experimentally determined structure factors, but the physical content of such models is limited [24].

The low temperature thermal properties of glasses have been found to be quite different from those of crystalline materials [25]. In particular, the lattice specific heat is anomalously large (compared to predictions based on measured sound velocities) and contains a linear term. These effects appear to be intrinsic to the glassy state. The anomalous linear specific heat seems to support the tunnelling models of Anderson et al. and Phillips [26]. Recently, much attention has focused on the specific heat of glasses at temperatures below 1K to observe this linear term [27]. These experiments have shown that the coefficients of this excess heat capacity are on the order of .05 mJ mol^{-1} K^{-2}, which is much smaller than a typical electronic term.

III. EXPERIMENTAL CONSIDERATIONS

III.1 RELAXATION METHOD AND APPARATUS

The experimental method used in this study is based on the relaxation time technique developed by Bachmann et al. [28]. The technique is illustrated schematically in Fig. 5. As shown, the sample is in thermal contact with a heat reservoir through a heat link having thermal conductance k. A measured amount of power is applied to the sample, thereby raising its temperature a small amount Δ_o above the reservoir temperature T_o. When thermal equilibrium is attained, the power to the sample is turned off and the sample temperature relaxes exponentially to that of the reservoir. The time constant of this relaxation is given by $\tau = C/k$, where C is the heat capacity of the sample. This process is analogous to the charging and discharging of a capacitor in a simple RC circuit. The situation can be described by a simple power balance relationship

$$P - \int_{T_o}^{T} k(T')dT' = C \frac{dT}{dt}$$

where P is the power into the sample, the integral describes the power out through the heat link, and the derivative term gives the time rate of change of heat in the sample. For small temperature changes $\Delta = T - T_o$, or for a linear thermal conductance,

$$P - k(T_{av})(T - T_o) = C \frac{dT}{dt} \qquad (6)$$

where $T_{av} = (T + T_o)/2$. In steady state,

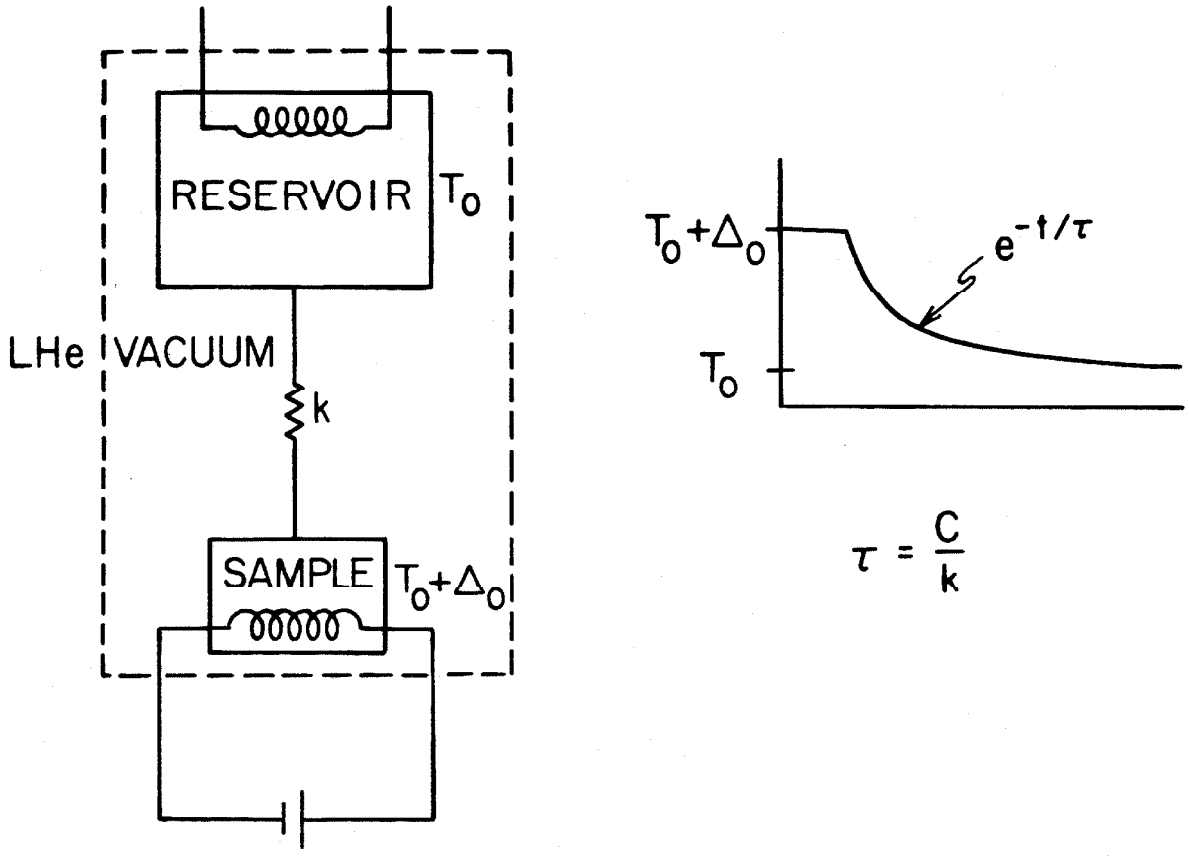

Figure 5. Schematic illustration of relaxation time technique.

$$\Delta = \Delta_o = \frac{P}{k(T_{av})}$$

and if at t=0, P → 0, then equation (6) has solution

$$T(t) = T_o + \Delta_o e^{-t/\tau}$$

with $\tau = C/k(T_{av})$. It is essential that Δ_o be kept small so that the temperature dependence of C over the range of Δ_o can be neglected.

To facilitate the relaxation time measurements, several sample holders like that shown in Fig. 6 were constructed. These holders consist of a copper support ring and a small sapphire bolometer linked to the six connectors on the copper ring by six fine wires. This copper fixture attaches to a mating fixture on a copper block, which forms the heat reservoir. A noninductively wound manganin wire heater on the block is used to vary the reservoir temperature. Samples, usually single splat-quenched foils or 5mm diameter cylindrical compacts, are bonded to the 5mm square sapphire bolometer; the wires support sample and bolometer and serve as the heat link from the sample to the reservoir. In addition to providing mechanical support for the sample, the wires are electrical leads for heater and thermometer elements on the bolometer.

The bolometers used are cut from sapphire wafers having thickness .25-.35 mm. Sapphire was chosen as the substrate material because of its high thermal conductivity and low heat capacity. Three pairs of Au contact pads are evaporated

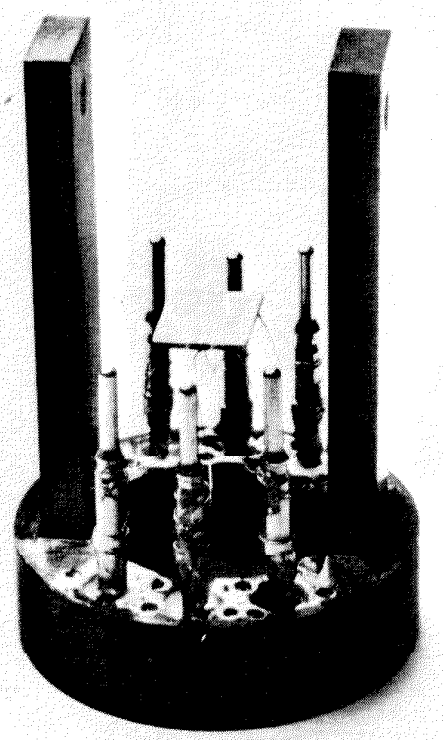

Figure 6. Sample holder comprising sapphire bolometer, copper supporting ring, and pin connectors. Height of the fixture is 3.5 cm.

onto the sapphire following the evaporation of a Cr adhesion layer. These form contacts for an evaporated Cr-Ti heater strip and two DAG low mass graphite resistance thermometers [29]. (Heater resistance is typically 500Ω - 2KΩ and is temperature independent.) Au-7% Cu wires having diameter .003" (.075mm) are attached to the contacts on the bolometer and to the pin connectors on the ring using conductive silver epoxy [30]. The epoxy forms a very strong bond ensuring that the leads do not detach during sample changes. The six pin connectors are anchored to the copper supporting fixture as shown in Fig. 7. Quartz bushings electrically insulate the pins from the copper holder while the thermally conducting grease [31] ensures good heat conduction. The grease also allows for the relatively high thermal expansion and contraction of the copper relative to the quartz.

This sample holder design offers low addenda, provides the necessary thermal isolation of the sample, and minimizes crosstalk between heater and thermometer elements. With several holders, samples can be mounted away from the probe and easily interchanged.

The components described above are contained in a vacuum can on a probe designed for measurements in a standard helium-4 cryostat. Electrical leads are brought down to the sample chamber through separate thin-wall stainless steel support tubes to minimize electrical crosstalk. Heat conduction from the room temperature end of the probe is reduced through the use of thin-wall tubing and by having the wires coiled several

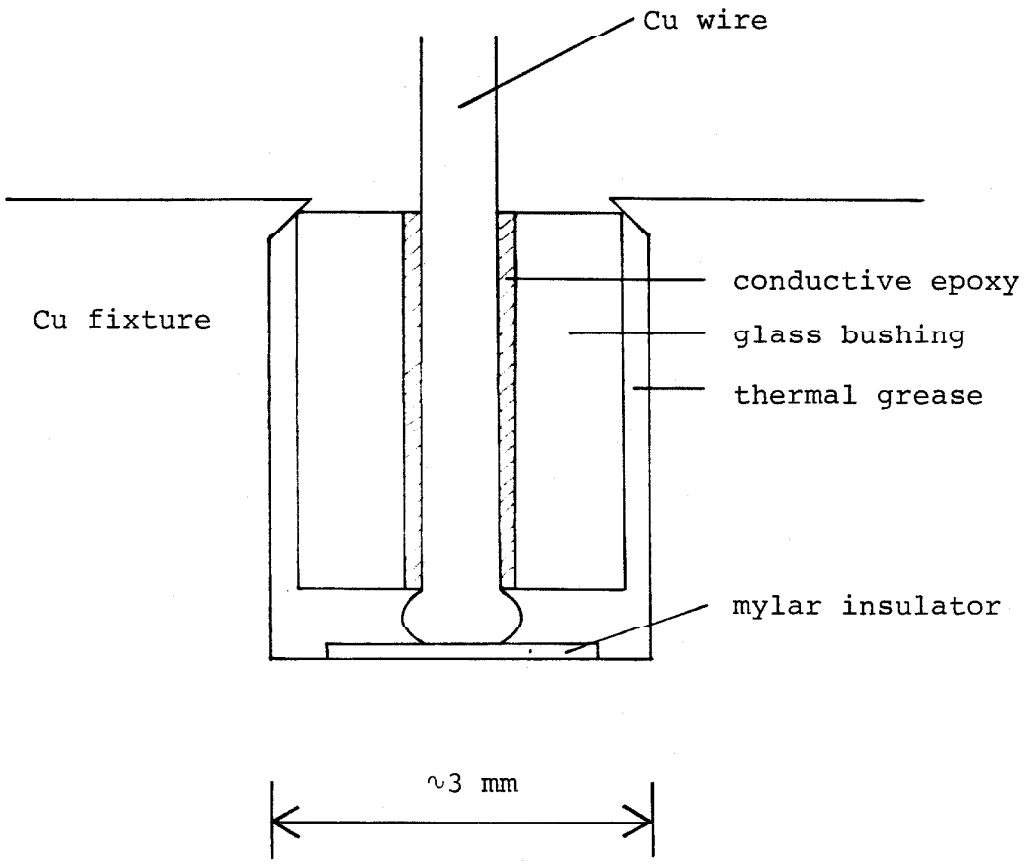

Figure 7. Detail of construction and anchoring of the six connectors on the sample holder. The pin connectors (not shown) are soldered to the Cu wires.

times in the sample chamber before contacting the block. The reservoir block itself is in thermal contact with the pumped liquid helium bath through an adjustable heat link. This makes it possible to quickly cool the apparatus to cryogenic temperatures without the use of an exchange gas and also stabilizes the block temperature when it is heated above the bath temperature. It is essential that the thermal conductance of this heat link be much greater than that of the wires linking the sample to the reservoir [28].

For temperature measurement, a calibrated carbon glass resistance thermometer mounted in the reservoir block is used. The resistance versus temperature characteristic of the carbon glass thermometer is shown in Fig. 8. This calibration has stayed constant over many cycles from room temperature to liquid helium temperature. A Lake Shore DTC500A temperature controller used with a silicon diode sensor provides regulation of the block temperature to within 5 mK.

A block diagram of the electronics used for measuring sample thermometer resistance and for recording cooling curves is shown in Fig. 9. The sample thermometer on the bolometer forms one arm of a Wheatstone bridge circuit which is driven by a 1500 Hz sinusoidal reference signal from a PAR HR-8 lock-in amplifier. A high precision 0-111KΩ adjustable resistor in parallel with an adjustable capacitor makes up the opposing arm of the bridge. The signal from the bridge circuit is amplified by a differential pre-amplifier and its output is

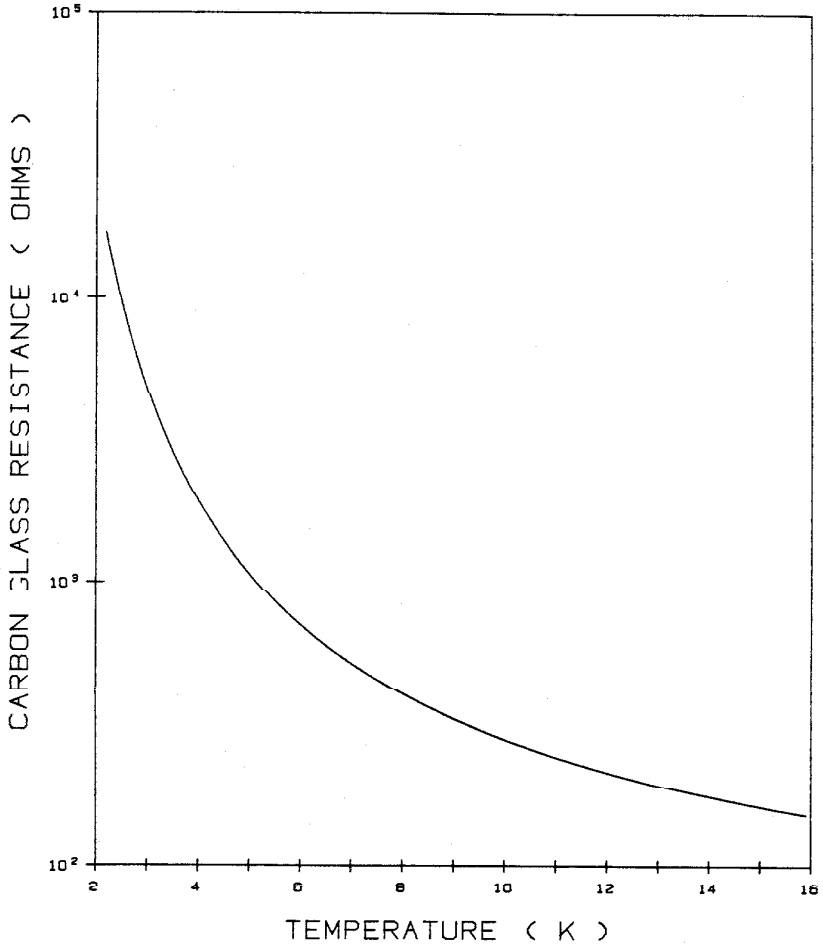

Figure 8. Carbon glass thermometer resistance versus temperature characteristic.

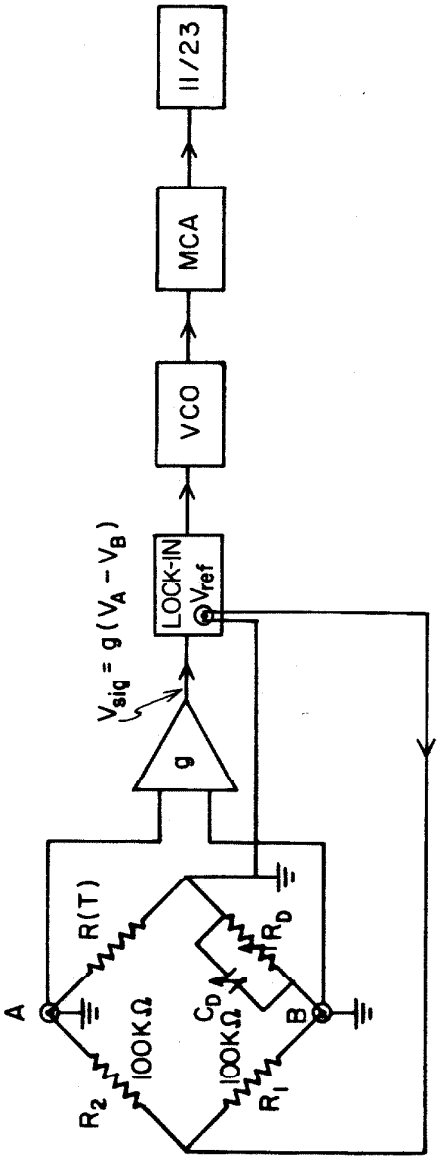

Figure 9. Block diagram of electronics used for determining sample thermometer resistance and for recording cooling curves.

phase detected by the lock-in. A null signal indicates a balance condition allowing the thermometer resistance to be read off the adjustable resistor. Near the balance condition, small changes in the resistance of the thermometer will produce a proportional signal at the output of the lock-in. Thus, a transient signal proportional to the sample temperature is obtained as the sample cools. However, if the integration time of the lock-in amplifier is comparable to the time constant of the exponential transient, the signal will be distorted by the bandpass characteristic of the lock-in. For this reason, the time constant of the lock-in must be much less than the time constant of the relaxation. The signal at the output of the lock-in is in turn converted to a series of pulses by a highly linear voltage controlled oscillator which produces a square wave of frequency 10-500 kHz proportional to the input signal voltage. These "pulses" are collected by a 1024-channel Canberra Series 30 Multichannel Analyzer operating in multi-channel scaling mode. The relaxation curves obtained in this manner are transferred to a PDP 11/23 computer and stored on floppy disks for later analysis. A typical relaxation curve shown in Fig. 10 demonstrates the signal-to-noise achievable. These data were collected on a 40 mg sample at approximately 6K.

A test of the apparatus on a standard sample was performed by measuring the heat capacity of a small sample of Cu, and comparing the results to published values [32]. Details of the experimental procedure are given in the next

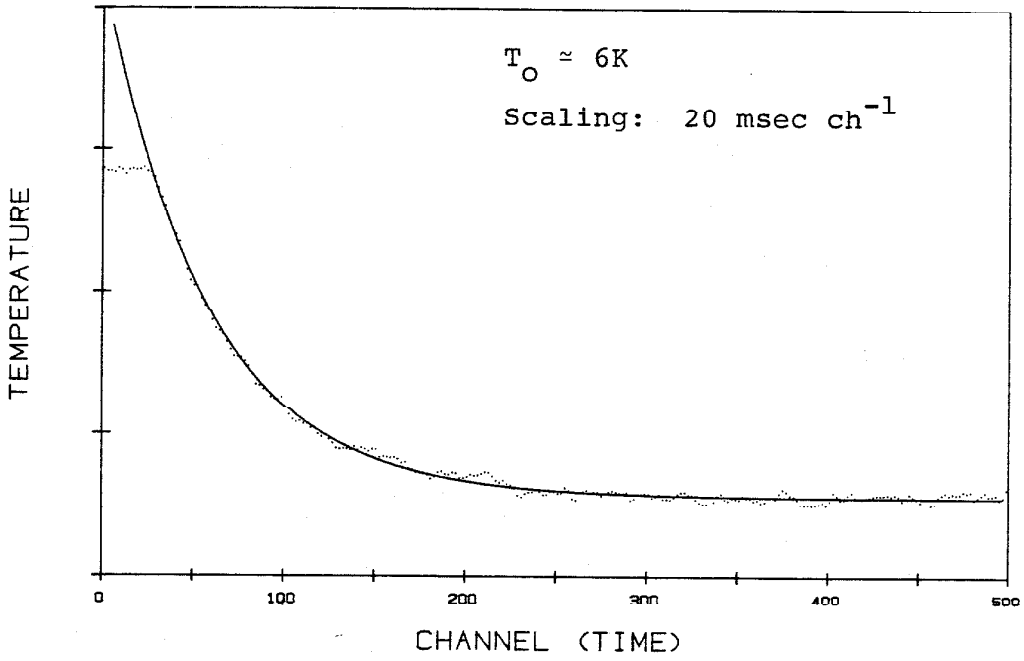

Figure 10. Typical sample temperature relaxation data. Solid line represents least-squares fit to $ae^{-t/\tau} + b$. Values from every second channel are shown. Full scale on the vertical axis is approximately 0.1 K.

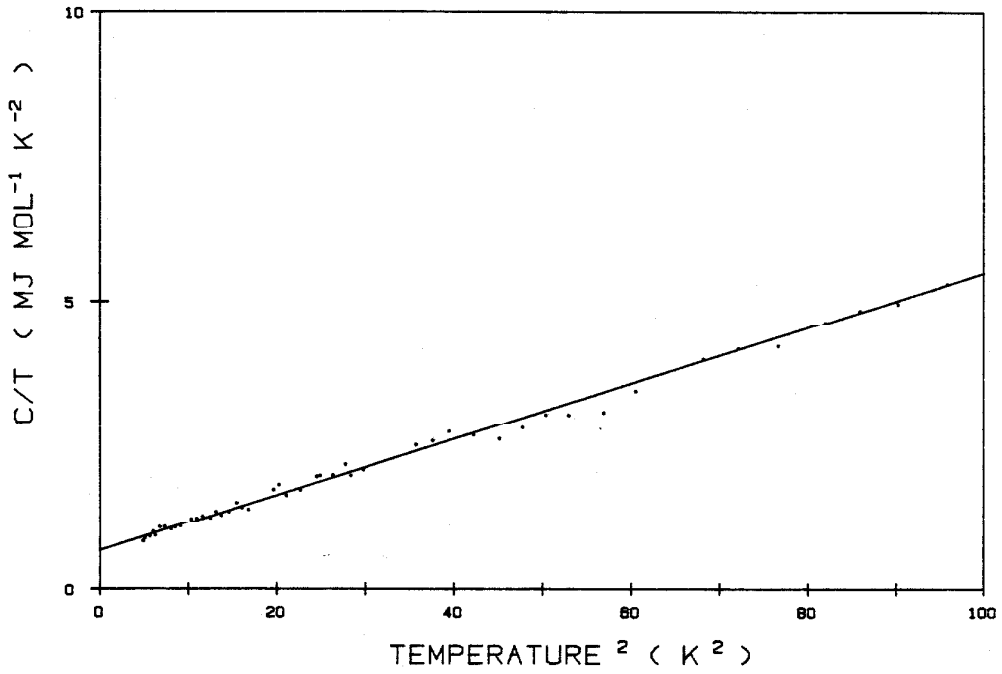

Figure 11. Measured specific heat of copper. Solid line is least-squares fit to $C/T = \gamma + \beta T^2$.

TABLE 1. Measured specific heat parameters for Cu.

	Measured	Standard [32]	
γ	0.65 ± 0.1	0.69	mJ mol^{-1} K^{-2}
θ_D	340 ± 5	343	K

section. The results obtained are shown in Fig. 11. Values of γ and θ_D obtained from these measurements are given in Table 1 along with values from the literature. The agreement is very good and indicates no systematic errors associated with thermometry. These results further indicate that the error in determining the absolute heat capacity with the apparatus is about 5% for a sample of this size.

III.2 EXPERIMENTAL PROCEDURE AND DATA ANALYSIS

In this section, we outline the procedure used to measure specific heat using the apparatus and method described above. We then describe how specific heat data are obtained from the raw data and examine the assumptions made in reducing the data.

A. Experimental Procedure

A sample is attached to the bolometer with a small measured amount (typically .1-.5 mg) of a thermally conducting binder. For most measurements reported here, the binder used was Apiezon 'N' grease [33]. The vacuum can is then sealed using an indium O-ring. The probe is leak tested with a mass spectrometer leak detector and pumped with a diffusion pump

for 1-2 days. During this time, the liquid helium cryostat is prepared. The heat capacity measurements are made point by point at roughly 0.2K temperature intervals from 2K to 12K. For superconducting samples, smaller intervals are used near the transition temperature T_c. The temperature range is determined by inherent limitations of the apparatus. Since the top end of the probe is at room temperature, the resultant thermal gradient down the probe causes heat to be conducted to the liquid helium bath. Thus, the reservoir temperature is always higher than that of the bath and this determines the minimum reservoir temperature. The upper limit is set by thermometry. Both the standard carbon glass thermometer on the block and the DAG thermometer on the sample become very insensitive above 15K.

The reservoir temperature is varied by adjusting the set point of the temperature controller or manually setting the heater current. At each temperature, the sample thermometer resistance is obtained by balancing the ac bridge. A balance condition is indicated by a null signal on the lock-in. These resistance values, along with readings of the standard carbon glass resistance are used for calibration of the sample thermometer. Because the DAG characteristic changes upon cycling to room temperature, it is necessary to recalibrate during each run. The sample is heated by passing a current through a series arrangement of the Cr-Ti heater on the bolometer and a standard resistance. The standard resistor voltage and the heater voltage are measured so that the power into the sample

at each temperature can be calculated. The sample power is typically on the order of 10^{-6} watts. With the sample heater on, the sample equilibrates at a slightly higher temperature; the bridge is again balanced and the resistance noted. The power is then turned off, and as the sample cools back to the reservoir temperature, the exponential transient signal is recorded. At all times, the lock-in time constant is maintained at less than 1/20 of the relaxation time constant of the sample. The heating and cooling of the sample is repeated so that at least two cooling curves are collected at each temperature. These are transferred to the computer and stored. Finally, the initial balance condition is verified.

The initial temperature throw Δ_o is constantly checked during the run and maintained at between .5 and 1% of the absolute temperature. (This value represents a trade-off between signal size and measurement accuracy.) This requires that the power to the sample be constantly increased as the temperature, and hence the thermal conductance of the lead wires, increases. As the heat link to the thermometers also increases with increasing temperature, they can dissipate larger amounts of power without significant self-heating. As a result, the carbon glass thermometer current used is 1 μA below 5K and 10 μA above 5K. The voltage driving the ac bridge is increased several times during the run as well. However, the sample thermometer power, which is typically on the order of 10^{-9} watts, is always much less than the heater power.

The raw heat capacity data will reflect contributions from the sample heat capacity and from that of the supporting addenda. The addenda heat capacity is determined in a separate run using the same procedure but with no sample. Once the heat capacity of a sample holder is known, it can be used for several samples. Occasionally, it has been found that the silver epoxy which is used for sample holder contacts ceases to conduct after several temperature cycles. When this occurs, addition of a very small amount of silver paint or epoxy restores the contact. Since this increases the addenda slightly, the sample holder heat capacity is remeasured. However, we have found that the addition of small amounts of paint produces no noticeable effect.

B. Data Analysis

The sample thermometer is calibrated by comparing the initial sample thermometer resistance readings to those of the calibrated carbon glass thermometer. This produces a set of values of (R_i, T_i). From this, temperatures at the top of the throw are obtained by Lagrangian interpolation:

$$T(R) = \sum_{i=1}^{n} T_i \prod_{\substack{j=1 \\ j\neq i}}^{n} \left(\frac{R - R_j}{R_i - R_j} \right) \quad .$$

A value of n=4 is generally used. This eliminates effects of changes due to thermal cycling since only data points taken close together are used for the interpolation. With

interpolated values for the temperatures at the top of the throw known, the temperature throw $\Delta_o = T_1 - T_o$ and the average temperature on the interval $T_{av} = (T_1 + T_o)/2$ can be calculated. Values of thermal conductance for the leads are now calculated from

$$k(T_{av}) = \frac{P}{\Delta_o} = \frac{V_H V_{std}}{R_{std}} \cdot \frac{1}{\Delta_o}$$

where V_H is the voltage across the heater during heating of the sample, V_{std} is the voltage across R_{std}, the standard resistance in series with the heater. In calculating heat capacity, these individual values of $k = P/\Delta_o$, or values taken from a polynomial least-squares fit to all of the thermal conductance data are used. It is desirable to use the individual values since no assumptions regarding the form of k(T) need be made. However, using fitted values helps to smooth the data and for smaller samples, fitted values are usually used.

A typical set of thermal conductance data is shown in Fig. 12. Experimentally, we have found that the thermal conductance of the six wires is well described below 10K by

$$k(T) \simeq a_o + a_1 T$$

where $a_o \simeq 0$ and $a_1 \sim 3 \times 10^{-6}$ watts K^{-2}. The steady state power balance for this simple form of k(T) is

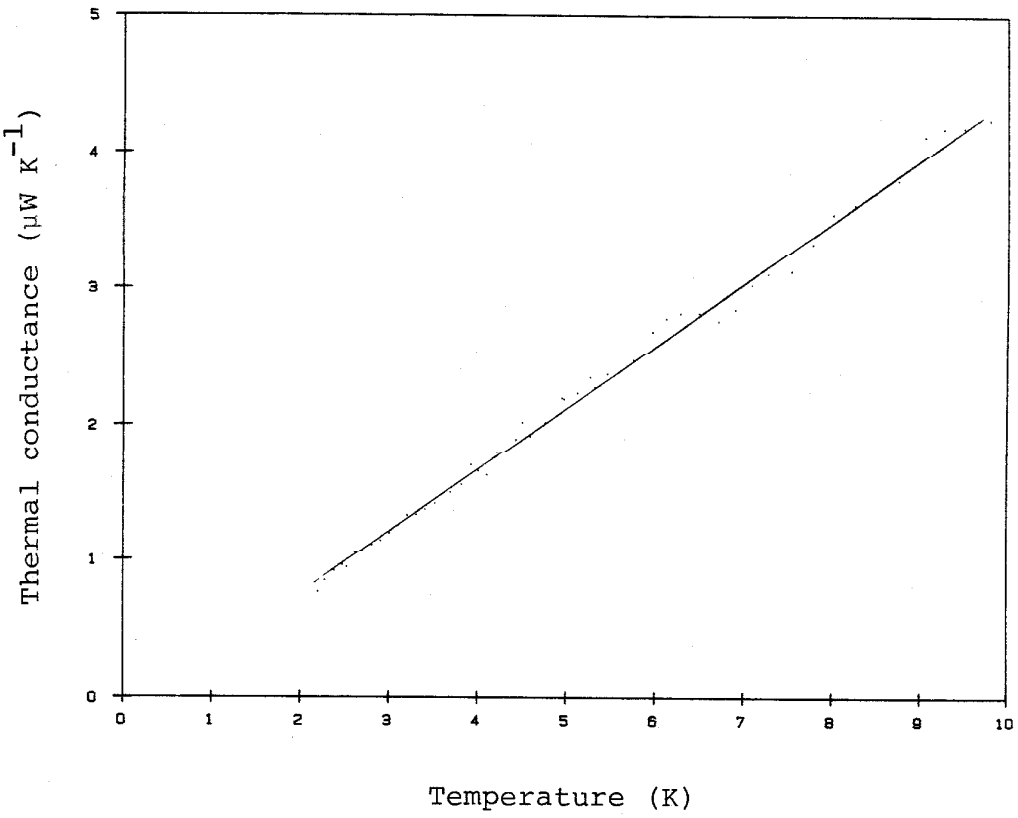

Figure 12. Thermal conductance of Au-7% Cu lead wires.

$$P = \int_{T_o}^{T_1} k(T')dT' = a_o(T_1 - T_o) + \frac{a_1}{2}(T_1^2 - T_o^2)$$

$$= k(T_{av})\Delta_o \quad .$$

Thus, for smooth data, the individual values should give the same result as the fitted values, independent of the size of Δ_o.

The relaxation curves, from which the time constants are obtained, are well described by a single exponential for the alloy samples used in the present study. This indicates that the thermal conductance of these samples is much greater than the thermal conductance of the leads. Hence, the curves can be fitted to the simple function $ae^{-t/\tau} + b$. This is accomplished by using a least-squares fit to a and b and a one-dimensional search to find τ. It is assumed here that for small temperature throws, the thermometer resistance is proportional to temperature. To check this assumption, the thermometer resistance can be expanded as

$$R(T) \simeq R(T_o) + \alpha(T - T_o) + \varepsilon$$

where

$$\alpha = \left.\frac{dR}{dT}\right|_{T_o}$$

and

$$\varepsilon = \frac{1}{2!}\left.\frac{d^2R}{dT^2}\right|_{T_o}(T - T_o)^2 + \ldots$$

To estimate the size of the error term ε, the resistance versus temperature characteristic of the sample thermometer

is fitted to the following polynomial in temperature:

$$R(T) = \sum_{n=0}^{9} A_n T^n$$

The derivatives $d^nR/dT^n\Big|_{T_o}$ can then be estimated. We have found that for temperature throws of 1% of the absolute temperature T_o the error ε is less than 1%. Thus, in most cases, R(T) is very linear and no correction is necessary. As noted previously, the temperature dependence of C(T) also produces errors of the order of Δ_o/T_o.

The final step in calculating the heat capacity is subtracting the heat capacity of the supporting addenda. For this, the measured sample holder heat capacity is fitted to a polynomial in temperature. Correction for the binders is made using values from the literature [34]. A set of heat capacity data (C_k, T_k) is thus generated where T_k is given by the value of T_{av} for the kth data point. The C_k are computed from $C_k = k(T_k)\tau_k - A_k$ where A_k represents the contribution of the addenda at T_k. The values of C_k are then normalized to the number of moles in the sample to obtain specific heat.

Subsequent analysis of the data involves fitting the normal state data to polynomials in temperature to obtain γ, β and higher order coefficients, calculation of the electronic entropy in the superconducting state, and extracting parameters such as T_C and the discontinuity at T_C. The fitting routines used employ a least-squares procedure in which the function

$$\Phi = \sum_{i=1}^{N} (f(x_i) - y_i)^2$$

is minimized for a set of N data points (x_i, y_i) and a given function f(x). To fit specific heat data (C_i, T_i) to a series in odd powers of temperature, the function $f(x) = \sum_{i=1}^{n} a_k x^k$ with $y_i = C_i/T_i$ and $x_i = T_i^2$ can be used. This gives

$$\Phi = \sum_{i=1}^{N} \left(y_i - \sum_{j=0}^{n} a_j x_i^j \right)^2$$

Minimizing Φ with respect to the a_j defines a system of n+1 equations:

$$\frac{\partial \Phi}{\partial a_k} = 0 \qquad k = 0, \ldots, n \ .$$

More explicitly,

$$\sum_{j=0}^{n} U_{k+j} \, a_j = V_k \qquad k = 0, \ldots, n$$

where

$$U_k = \sum_{i=1}^{N} x_i^k \qquad \text{and} \qquad V_k = \sum_{i=1}^{N} y_i \, x_i^k \ .$$

Solution of the system gives the optimum a_j. For example, fitting to $C = \gamma T + \beta T^3$ corresponds to solving the above with n=1, $\gamma = a_o$ and $\beta = a_1$.

In analyzing data on superconducting samples, we wish to calculate the electronic entropy at T_c from the data below T_c. To do this, we fit a small number (~ 10) of data points at the lowest temperatures to $C = a_1 \exp(-a_2/T)$ after subtracting the

lattice contribution. For purposes of this calculation, this is merely a convenient form to use for extrapolating the data to T=0. Defining T_{min} as the lowest temperature at which there is a data point, we obtain the entropy at T_{min} from the fitted values a_1 and a_2:

$$S = \int_o^{T_{min}} \frac{a_1 e^{-a_2/T}}{T} dT$$

$$= a_1 \left(- \gamma - \ln z - \sum_{n=1}^{\infty} \frac{(-1) z^n}{n n!} \right)$$

where $z = a_2/T_{min}$ and γ is the Euler constant = .577216... [35]. The latter expression is a series representation of the exponential integral E_1. The series converges rapidly and is easily evaluated. The remaining contribution to the entropy at T_C is gotten by numerically integrating the data from T_{min} to T_C using the formula

$$\int_{T_{min}}^{T_C} \frac{C}{T} dT = \frac{1}{2} \sum_{j=2}^{N} (T_j - T_{j-1}) \left(\frac{C_j}{T_j} + \frac{C_{j-1}}{T_{j-1}} \right) .$$

III.3 SAMPLE PREPARATION

The samples used in this study were a 3/16" diameter cylindrical piece of pure Cu and amorphous foils having composition $(Mo_{.60}Ru_{.40})_{100-x}B_x$ where x = 14, 16, 18, 20 and

22, and $(Mo_{.60}Ru_{.40})_{100-x}Si_x$ where x = 24, 26, 28 and 30. Measurements were made on foils as-quenched.

The Cu sample was prepared from 3/16" diameter Cu rod of purity 99.995%. The mass of this sample after machining was 253.8 mg. Prior to mounting, it was kept sealed under vacuum to prevent oxidation.

Ingots of Mo-Ru-B and Mo-Ru-Si were prepared by levitation melting of those elements by rf heating on a water-cooled silver boat under an argon atmosphere. Purity of the starting materials was Mo, 99.99%, Ru, 99.98%, B, 99.999%, and Si, 99.99%. The uncertainty in metalloid concentration in these ingots is less than 0.5%. Foils were subsequently prepared from these ingots by rapidly quenching from the melt with a piston-and-anvil apparatus. The foils obtained were typically 1-2 cm in diameter and between 30 and 60 μm in thickness. The amorphous nature of the foils was verified by x-ray scanning using a Norelco diffractometer. Cu K_α radiation (λ = 1.542 Å) was used to scan foils from $2\theta = 30°$ to 80° at a rate of 0.125° min^{-1}. Samples which showed evidence of crystallinity were not used for heat capacity measurements. A typical x-ray pattern is shown in Fig. 13. Before measurements are made, copper from the piston and anvil faces of the splat-quenching apparatus was removed from the surface of the foils by briefly soaking them in a strong aqueous solution of HNO_3. The surfaces were then cleaned with acetone and methanol to remove residual greases.

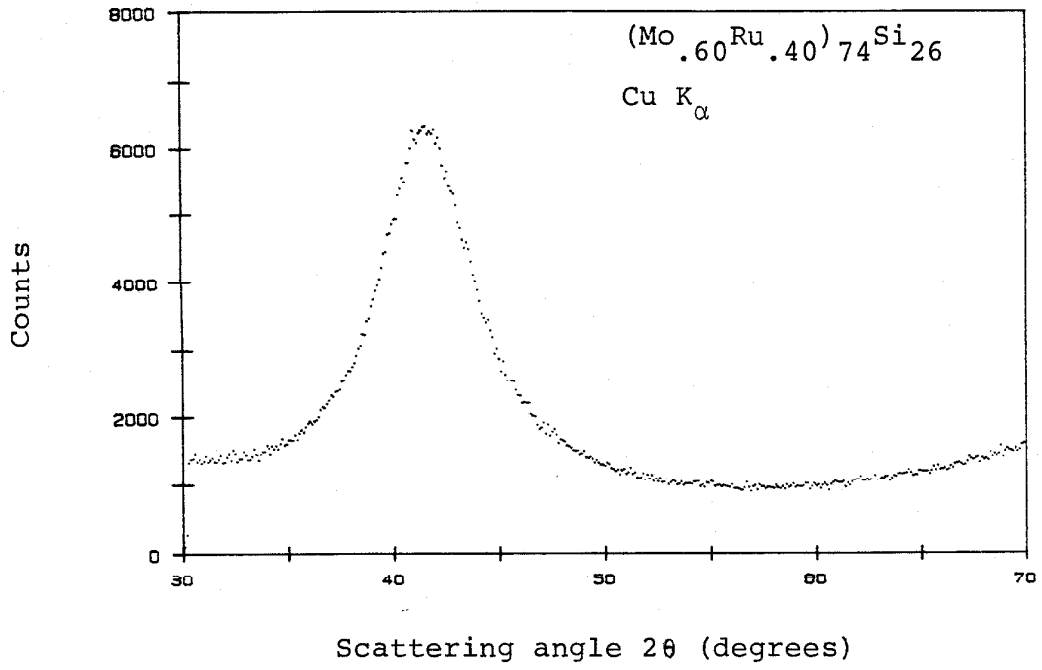

Figure 13. Typical x-ray diffraction pattern for amorphous Mo-Ru alloy.

The sample holders accommodate samples up to 1/2" in diameter so it was sometimes necessary to cut larger foils. The mass of the foils after cutting ranged from 20-60 mg. Two of the Mo-Ru-B samples used were made from several foils bonded with GE7031 varnish [36]. The foils were powdered using a tungsten carbide mortar and pestle and pressed under high pressure into cylindrical pellets. The mass of such a sample was about 200 mg.

IV. RESULTS AND DISCUSSION

IV.1 LOW TEMPERATURE SPECIFIC HEAT OF Mo-Ru-B ALLOYS

We have used the relaxation time method to measure the heat capacity of transition metal-metalloid glasses having composition $(Mo_{.60}Ru_{.40})_{100-x}B_x$ where x = 14, 16, 18, 20, and 22% boron [37]. These measurements cover most of the compositional range over which the alloys can be made amorphous. Our results, primarily in the composition dependence of the density of states at the Fermi level, indicate the existence of a "phase" boundary in the middle of this compositional range. Previous work on this alloy system has shown that certain properties--electrical resistivity, nearest neighbor distance of the metal atoms and ^{11}B NMR linewidth--change discontinuously near 18% B [38,39]. The behaviour of the resistivity is shown in Fig. 14. In addition, the high boron alloys are considerably more brittle [38]. This composition dependence has been interpreted in terms of changes in the defect structure of the material, which is consistent with an overall structural transition. The present specific heat results also show that these alloys are intermediate coupled superconductors whose thermal behaviour is in accord with the BCS theory of superconductivity.

Heat capacity is measured using the method and procedures outlined in the previous chapter. Measurements were made at temperatures ranging from 2K to 15K on as-quenched single foils, or on compacts made from several foils. Masses of the samples ranged from about 25 mg for a small single foil to about 200 mg for a compact. Samples were bonded to the

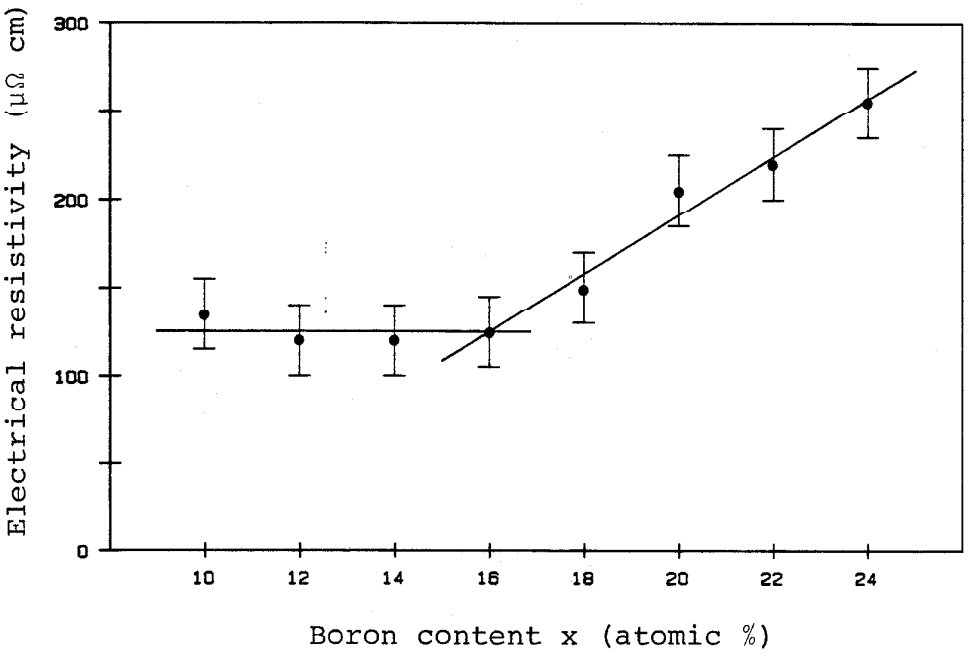

Figure 14. Electrical resistivity of $(Mo_{.60}Ru_{.40})_{100-x}B_x$ as a function of boron content x. (Values taken from reference 38.)

sample holder bolometer with Wakefield thermal compound or Apiezon 'N' grease. At 4.2K, the total addenda heat capacity represented about 40% of the measured heat capacity for the smallest sample and about 5% for the largest sample.

The specific heat data for the Mo-Ru-B alloy series are presented in Fig. 15. Normal state and superconductivity parameters obtained from this data set and from a second measurement on $(Mo_{.60}Ru_{.40})_{82}B_{18}$ shown in Fig. 16 are given in Tables 2 and 3. Normal state parameters are derived from a least-squares fit of the data above the superconducting transition to the polynomial $C(T) = \gamma T + \beta T^3 + \delta T^5$. As discussed in Chapter II, the coefficient of the first term is related to the density of states at the Fermi level through the relation

$$\gamma = \frac{2}{3} \pi^2 k_B^2 N(\varepsilon_F)(1 + \lambda) \quad .$$

In this treatment, we neglect effects of non-electronic origin which may also lead to a specific heat which is linear in T. The contribution of such terms to γ is generally quite small [27]. The Debye temperature is calculated from

$$\theta_D = \left(\frac{1944}{\beta}\right)^{1/3}$$

where β is in J mol^{-1} K^{-4} and θ_D is in degrees K. It is evident that the data deviate from the simple Debye T^3 law for temperatures greater than $\theta_D/30$ and we include the T^5 term for fitting data above 10K. This non-Debye like behaviour has been observed in several metal-metalloid glasses [40].

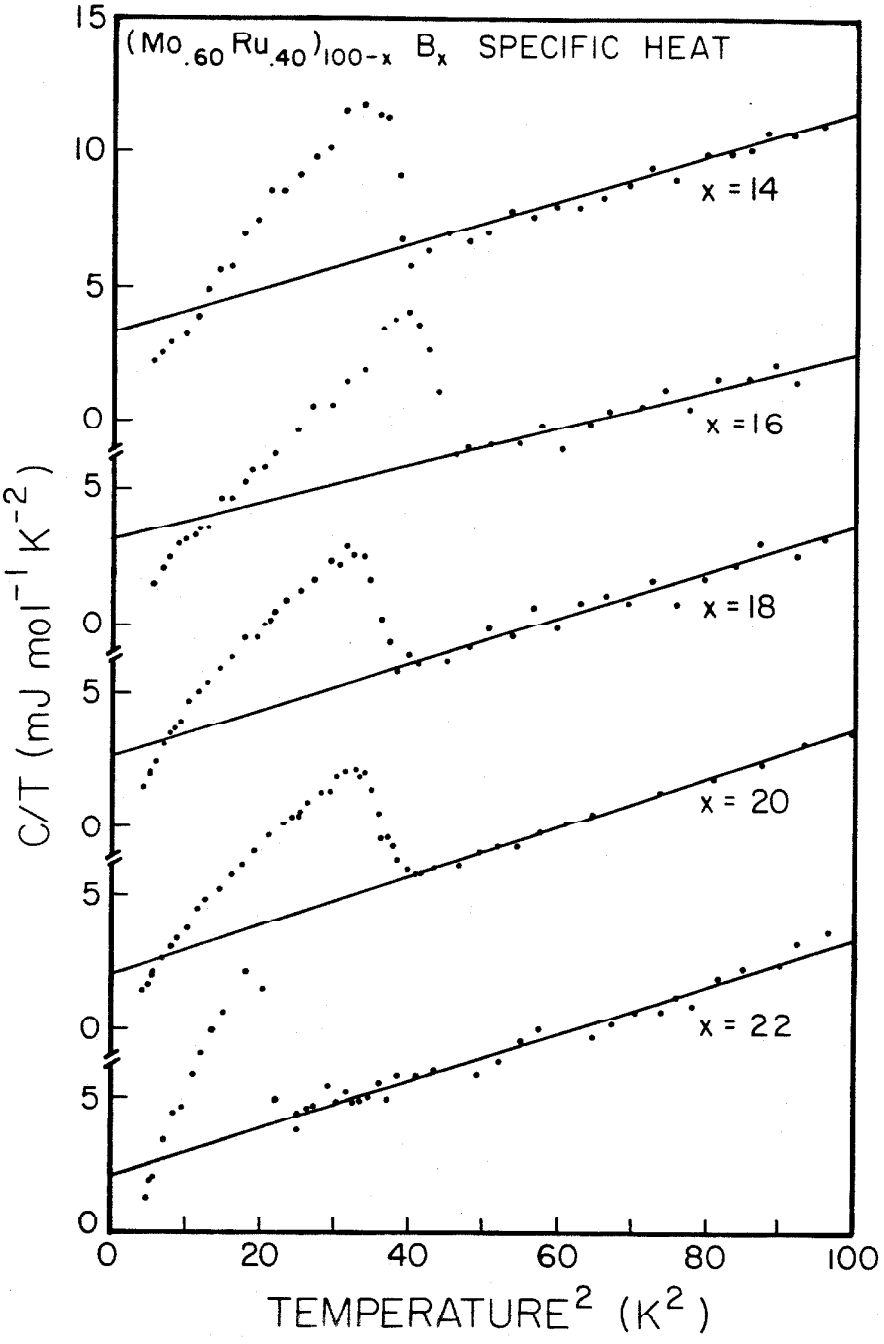

Figure 15. Specific heat data for $(Mo_{.60}Ru_{.40})_{100-x}B_x$ metallic glasses.

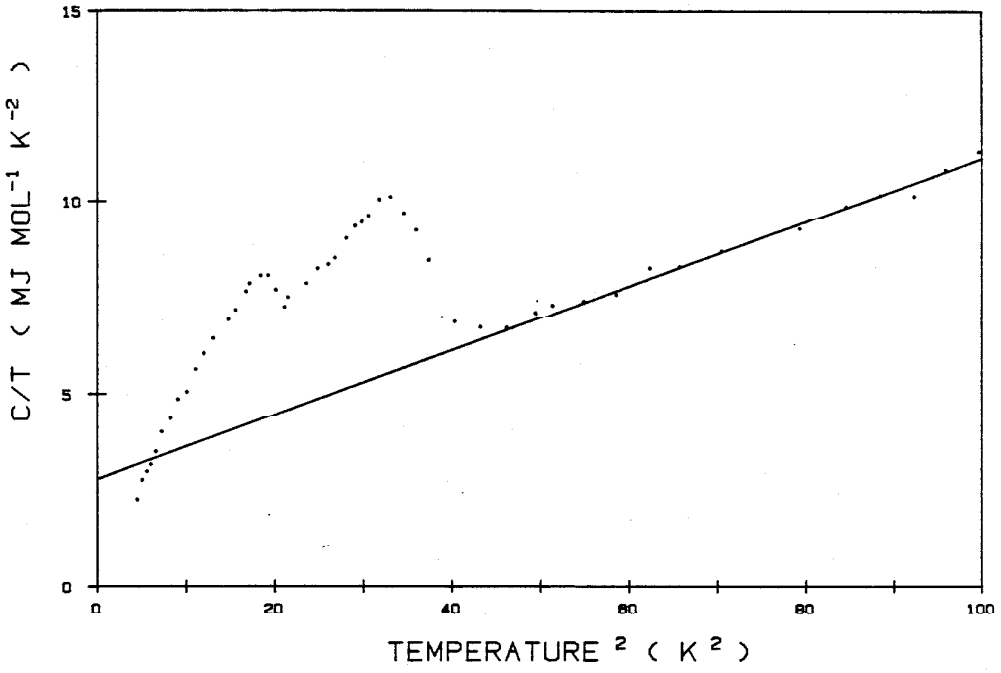

Figure 16. Specific heat data for $(Mo_{.60}Ru_{.40})_{82}B_{18}$ sample (2) showing two superconducting transitions.

TABLE 2. Normal state parameters for $(Mo_{.60}Ru_{.40})_{100-x}B_x$

x(%B)	γ(mJ mol^{-1} K^{-2})	θ_D(K)
14	3.4	295
16	3.1	301
18 (1)	2.6	283
(2)*	2.8	286
20	2.0	277
22	2.1	280

*Two-phase material

TABLE 3. Superconductivity parameters for $(Mo_{.60}Ru_{.40})_{100-x}B_x$.

x(%B)	T_c(K)	λ	$\Delta C/\gamma T_c$	B(K)	B/T_c
14	6.3	0.69	1.4	9.67	1.55
16	6.4	0.69	1.7	9.87	1.54
18 (1)	6.1	0.69	1.5	9.39	1.55
(2)*	4.7,6.1	--	--	--	--
20	5.9	0.69	1.9	9.10	1.54
22	4.7	0.64	2.0	8.8	1.8
BCS	--	--	1.43	$1.44T_c$	1.44

*Two-phase material

Values given in Table 3 for the superconducting transition temperatures of the alloys are taken at the midpoint of the transition, after subtracting the lattice contribution. The McMillan equation for the transition temperature [15], in the form

$$T_C = \frac{\theta_D}{1.45} \exp -\left[\frac{1.04(1+\lambda)}{\lambda - \mu^*(1+0.62\lambda)}\right]$$

is used to calculate λ, using $\mu^* = 0.13$. Values of $\Delta C/\gamma T_C$ represent the normalized discontinuity in the electronic specific heat at the transition. It should be noted that this quantity can only be calculated to an accuracy of about 25% owing to errors in determining γ and ΔC. The entropy at T_C is given by

$$S(T_C) = \int_0^{T_C} \frac{C(T)}{T}\, dT \quad .$$

The value of $S(T_C)$ must be the same whether calculated by extrapolating the polynomial fit to $T = 0$ or if derived from the data below T_C. This provides a self-consistent check on the fit which is evidently well-satisfied by our fitting procedure; values of γ derived from the integral of the data below T_C are within 10% of values derived from the polynomial fit. This is comparable to the uncertainty in the fitting parameter. In calculating $S(T_C)$ using the data below T_C, it is necessary to extrapolate the data to $T = 0$. This is accomplished by fitting the electronic specific heat at the lowest temperatures to the expression $C = Ae^{-B/T}$. The fitting

parameter B can then be used to compare the data to the approximate BCS relation for the heat capacity of the superconducting electrons given in equation (5) in Chapter II.

The most striking feature of the data above T_C is the rapid decrease of γ as the boron content in the alloy series increases. As shown in Table 3, the electron-phonon coupling constant γ shows little variation as a function of x. Hence, the density of states at the Fermi level must be changing rapidly as well, in the region around x = 18% B. Additional evidence for this trend is given by values of γ calculated from the measured gradient of the upper critical field. In convenient units,

$$\gamma = \frac{2.23}{\rho\alpha} \left.\frac{dH_{C_2}}{dT}\right|_{T_C} \qquad (7)$$

where ρ is the normal state resistivity in $\mu\Omega$ cm, α is the density in mol cm^{-3} and the gradient is measured in kOe K^{-1}. Values of γ derived from specific heat measurements and derived from upper critical field and resisitivity measurements are plotted as a function of boron content x in the lower part of Fig. 17. (The values of ρ and $dH_{C_2}/dT\,|_{T_C}$ used are taken from reference 38). The agreement is very good, and we conclude that equation (7) above can be used to estimate $N(\varepsilon_F)$ in these materials in the absence of specific heat data. The variation of the limiting Debye temperature θ_D is plotted in the upper part of Fig. 17. For the data from samples with x = 14, 16, and 18% boron, where measurements were taken to

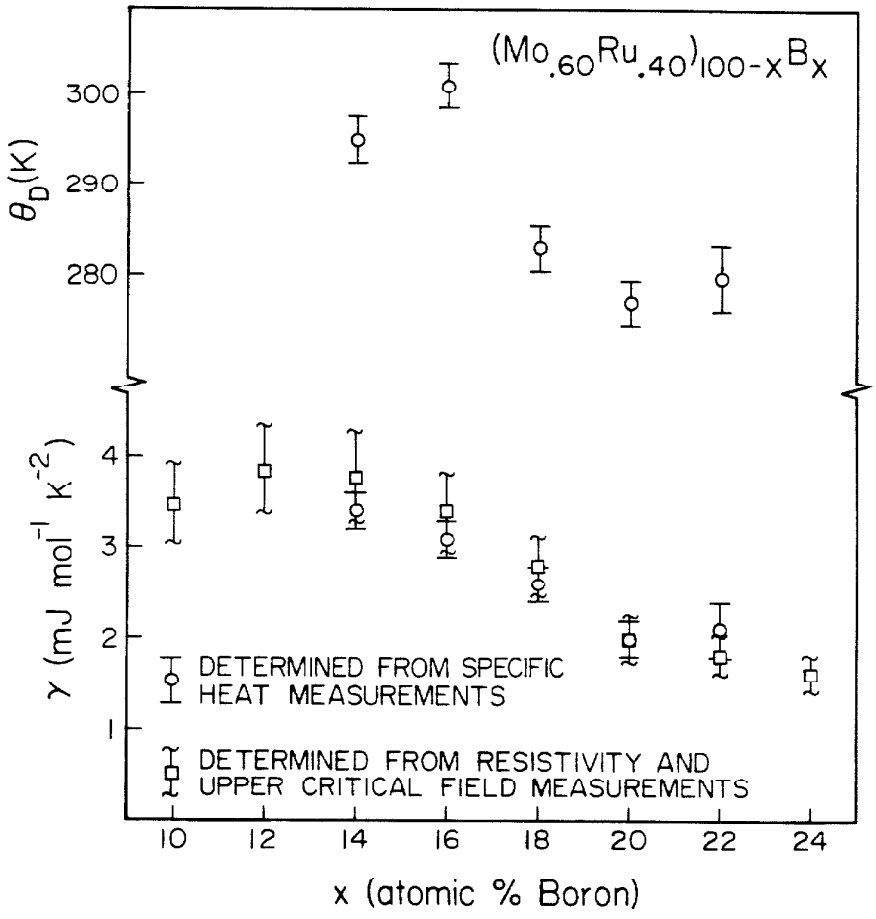

Figure 17. Composition dependence of the Debye temperature θ_D and electronic specific heat coefficient γ of amorphous $(Mo_{.60}Ru_{.40})_{100-x}B_x$ alloys.

higher temperatures, the best fit was obtained using a T^5 term. θ_D generally decreases across the series but appears to change discontinuously from an average value of about 300K for $x < 18\%$ to an average value of about 280K for $x \geq 18\%$. The value of θ_D obtained for $(Mo_{.60}Ru_{.40})_{82}B_{18}$ of 283K agrees with the Debye temperature for this alloy determined from Mossbauer studies of Fe-doped Mo-Ru-B [41,42].

Estimates of the ratio B/T and of $\Delta C/\gamma T_c$, the jump in the electronic specific heat at the transition, are within experimental errors of values predicted by the BCS theory of weak-coupled superconductors [11]. Like many transition metal superconductors, the electron-phonon coupling in these materials appears to be weak to intermediate [43]. This is also reflected in values of the coupling constant computed from the McMillan equation. Values of the superconducting transition temperature T_c shown in Table 3 are in good agreement with previously reported values of T_c for Mo-Ru-B measured inductively and resisitively [38].

In Figure 16, specific heat data obtained from a second sample with x = 18% are presented. The γ and θ_D values agree with those of the other sample of this composition but the specific heat clearly shows the presence of two superconducting phases. The transition temperatures of the two phases are 6.1K and 4.7K. The sample used was a compact made from several foils. Following the heat capacity measurements,

this sample was analyzed with additional x-ray diffraction, transmission electron microscopy, and Mossbauer spectroscopy in an attempt to discover the nature of the second phase. Depression of T_c by magnetic Fe impurities was ruled out by Mossbauer measurements, which showed no evidence of Fe [44]. This places an upper limit on the Fe content of .03% by weight, which could depress the transition temperature by no more than 0.7K [45]. Extensive x-ray diffraction and TEM showed no evidence of crystallinity in the sample and thus the low T_c peak in the specific heat curve could not be associated with a crystalline phase. Measurements of T_c on samples of related crystalline borides Mo_2B and Ru_7B_3 gave further support to this assumption. We obtain values of 3.8K and 3.2K respectively, for the transition temperatures of these materials measured inductively; both are much lower than the 4.7K observed in the 18% B sample. We cannot discount the possibility that one of the foils in the compact had the wrong composition. However, this seems unlikely as great care was taken with all samples.

IV.2 LOW TEMPERATURE SPECIFIC HEAT OF Mo-Ru-Si ALLOYS

As a companion study to the heat capacity measurements on Mo-Ru-B, we have determined the specific heat of a similar group of alloys having composition $(Mo_{.60}Ru_{.40})_{100-x}Si_x$. The silicon content of these alloys ranges from x = 24% to 30%. All samples were single foils prepared by rapid quenching. The masses of the foils used are given in Table 4. The

foils were bonded to the bolometer using 0.1 to 0.2 mg of Apiezon 'N' greases. The binder heat capacity is accounted for using literature values and typically represents from 5% to 20% of the total measured heat capacity, depending on the temperature. The total addenda heat capacity is equivalent to that of roughly 15 mg of Mo-Ru-Si.

The specific heat data up to T = 10K is given for all alloys considered in Fig. 18. The data from 2K to 10K were analyzed to obtain the parameters shown in Table 4. Normal state data above the transition temperature were fitted to the polynomial $C = \gamma T + \beta T^3$ to obtain γ and θ_D values. These are plotted as a function of silicon content in Fig. 19. Values of T_C were taken at the midpoint of the transition. From θ_D and T_C, the electron-phonon coupling constant λ was calculated using the McMillan relation. For alloys with 28% and 30% Si, the transition occurs at too low a temperature to allow a meaningful fit to be obtained for the data below T_C. For the other alloys, for which there are several points below T_C, the data were fitted to $C = Ae^{-B/T}$ providing an extrapolation of the data to T = 0 so that the electronic entropy could be computed. For those alloys where $S(T_C)$ could be calculated, the values of γ and θ_D determined from the fit were consistent with the thermodynamic constraint on $S(T_C)$.

As shown in Fig. 19, γ decreases with silicon content x while θ_D increases. This results in decreasing values of λ as x is increased. Hence, the bare density of states at the Fermi level, normalized by a factor of $(1 + \lambda)$, decreases

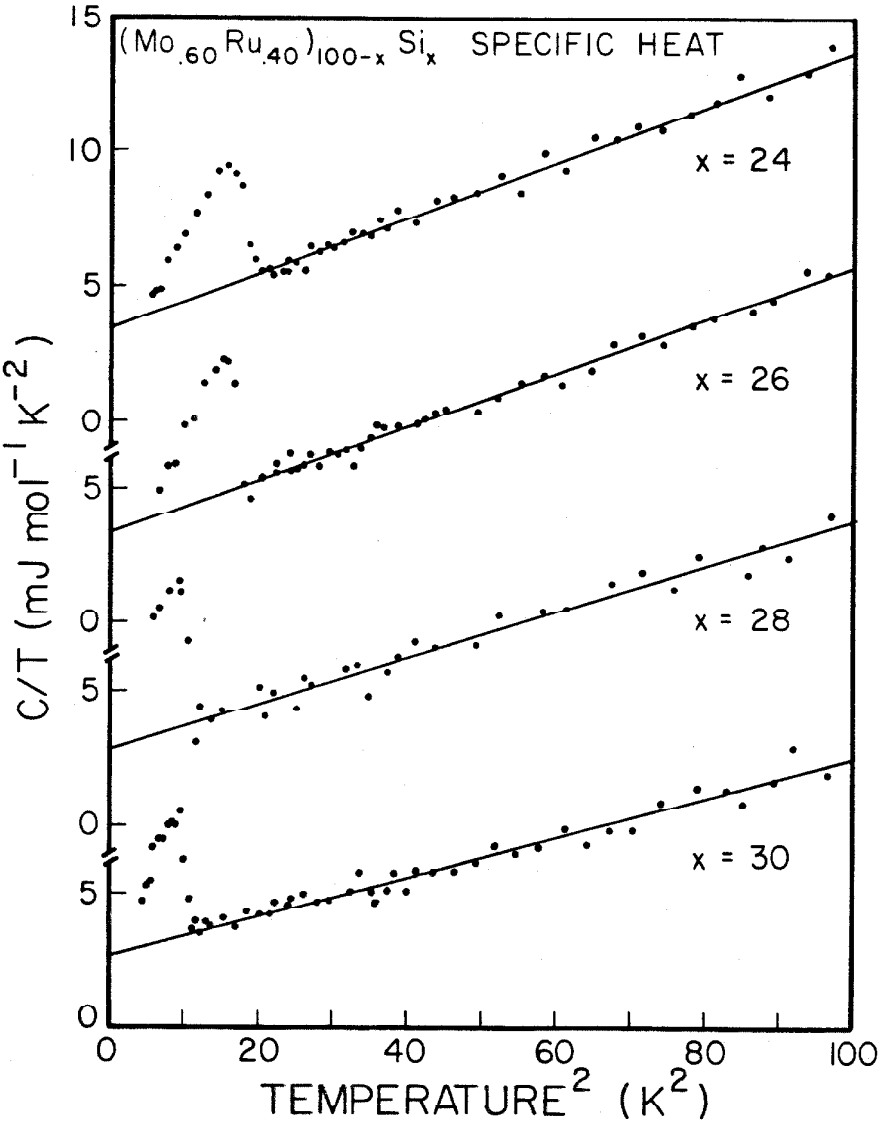

Figure 18. Specific heat data for $(Mo_{.60}Ru_{.40})_{100-x}Si_x$ metallic glasses.

TABLE 4. Parameters derived from $(Mo_{.60}Ru_{.40})_{100-x}Si_x$ specific heat data.

x	Sample Mass (mg)	γ(mJ mol^{-1} K^{-2})	θ_D(K)	T_C(K)	λ	$\Delta C/\gamma T_C$
24	42.3	3.4	265	4.3	0.63	1.3
26	42.6	3.2	270	4.1	0.62	1.5
28	26.8	2.8	284	3.4	0.58	1.7
30	30.5	2.6	297	3.2	0.57	1.6

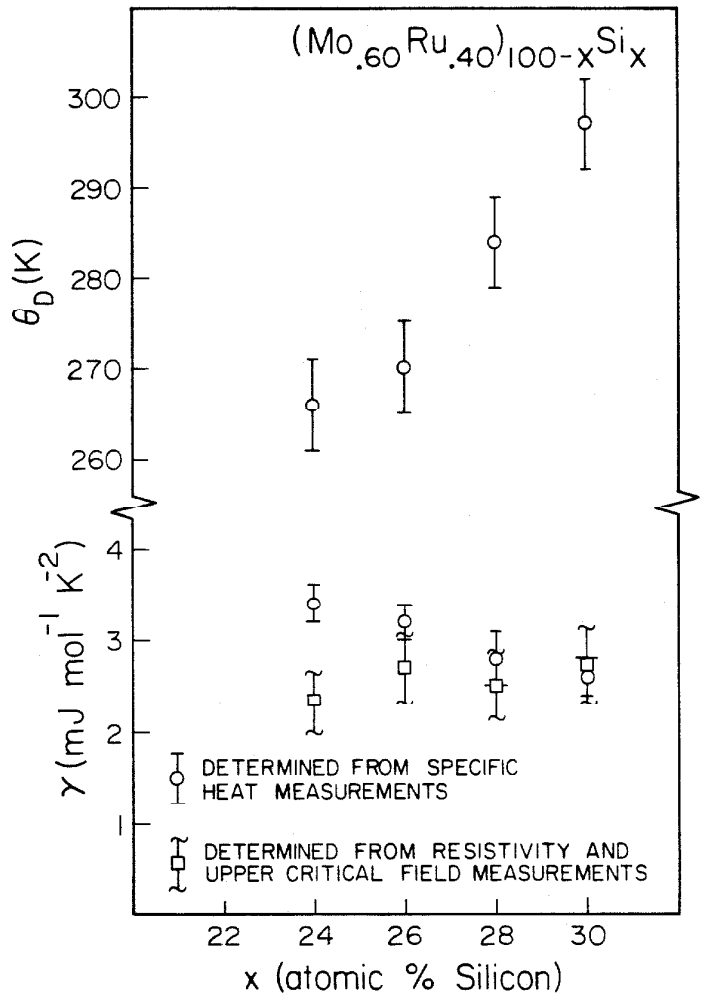

Figure 19. Composition dependence of the Debye temperature θ_D and electronic specific heat coefficient γ of amorphous $(Mo_{.60}Ru_{.40})_{100-x}Si_x$ alloys.

slowly for this series as the metalloid content is increased. γ values calculated from upper critical field gradient and resistivity do not agree well with the trend in γ that is observed in specific heat. (Values of ρ and $dH_{C2}/dT\,\big|_{T_C}$ used to prepare Fig. 19 are taken from reference 38.)

As with the Mo-Ru-B alloys, values of $\Delta C/T_C$ obtained for Mo-Ru-Si are within experimental errors of the BCS value of 1.43.

IV.3 COMPARISON WITH RELATED PHASES

For comparison, results are presented in Table 5 for crystalline σ-phase $Mo_{61}Ru_{39}$ [46], body-centred cubic $Mo_{70}Ru_{30}$ [47], and amorphous thin-film $Mo_{58}Ru_{42}$ [48]. The values of γ and T_C for these alloys follow the trends that we observe for splat-quenched amorphous Mo-Ru-B and Mo-Ru-Si alloys. The T_C (6.7K) for $Mo_{70}Ru_{30}$ is somewhat low, but in the bcc Mo-Ru alloys, T_C increases with increasing Ru content [47] and could be >8K for a bcc $Mo_{60}Ru_{40}$ alloy. The Debye temperature of the thin film $Mo_{58}Ru_{42}$ sample is quite low for a 4d-4d alloy [49] and it would appear that this may not be representative of bulk melt-quenched Mo-Ru-metalloid alloys. Using the McMillan formula, one calculates a value of $\lambda = .84$, indicating a more strongly coupled superconductor. However, the θ_D values of alloys with x < 18% B and of all Si alloys appear to increase with addition of metalloid atoms. Thus the thin film material may have a similar type of lattice. Also, linearly extrapolating the T_C values of Mo-Ru-B to x=0 yields

TABLE 5. Properties of related Mo-Ru phases.

	γ	T_C	θ_D	λ	B/T_C	Ref.
σ $Mo_{61}Ru_{39}$	4.11	7.2	418	0.65	1.50	46
bcc $Mo_{70}Ru_{30}$	3.9	6.7	435	0.62	--	47
$Mo_{58}Ru_{42}$	4.9	8.3	238	0.84	--	48

a value of 8.6K which is close to the value of 8.3K observed for $Mo_{58}Ru_{42}$.

IV.4 DISCUSSION

A. Structure and Properties

It has been reported previously that certain properties of $(Mo_{.60}Ru_{.40})_{1-x}B_x$ alloys show marked changes as a function of boron content at around x = 18% boron [38]. In particular, the normal state electrical resistivity has been shown to be independent of x below x = 18% and to increase rapidly for x > 18%. Based on the specific heat results presented here, there is strong evidence for a significant structural change near 18% boron which can be correlated with the resistivity behaviour.

Firstly, both specific heat and upper critical field data for the Mo-Ru-B alloys indicate a change in $N(\varepsilon_F)$ by almost a factor of two as the boron content changes from 14% to 22%. Also, the Debye temperature appears to change discontinuously in the middle of the range. The latter may indicate a modification of the lattice structure since the composition range is small, but such variations are not uncommon in alloy systems. However, the change in $N(\varepsilon_F)$ implies a change in structure which strongly modifies the total density of states. The effect is too large to be accounted for in a rigid band picture. Unless the density of states contains sharp features like that of a crystalline transition metal [50], then a very large change in the electron-to-atom

ratio (e/a) would be needed to account for the changes in $N(\varepsilon_F)$ resulting from shifts of ε_F. Owing to the large energy width $\Delta\varepsilon$ of an electron state in the amorphous solid due to disorder-induced scattering, it is expected that the density of states of a glass would not contain sharp structure [51]. Thus the addition of a relatively small number of metalloid atoms could not change e/a enough without significant charge transfer between the metal d bands and the metalloid s-p bands. Such effects are not expected in view of the similar electronegativities of the constituent atoms in Mo-Ru-B: for Mo, the electronegativity is 2.2; for Ru, 2.2; and for B, 2.0 [52].

In transition metal alloys, the dominant contribution to the total density of states $N(\varepsilon)$ comes from d-bands. From a tight-binding analysis of the d-band contribution to $N(\varepsilon_F)$, it is expected that the d-band partial density of states $N_d(\varepsilon_F)$ will largely be determined by the local environment of the transition metal atoms [2]. Hence the observed Fermi-level total density of states for Mo-Ru-B should reflect the short-range order of the metal atom environment; that is the number and type, directions and separations of atoms around the Mo and Ru atoms in the glass. The behaviour of γ as a function of x shown in Fig. 17 suggests one type of short-range order for $x < 16\%$ boron and the dominance of another type of short-range order for $x > 20\%$ boron. This behaviour is similar to that which occurs when crossing compositional phase boundaries in crystalline alloys. In a

binary alloy system, one typically observes transitions from single phase material to two phases and back to a single phase with varying composition. In a crystalline material, this is accompanied by a change in long-range order. For amorphous phases, the variation of composition could produce a similar change in the short-range order. That is, one could progress from a material having one predominant short-range order to a mixture of two structures and finally back to a material with predominantly the second type of short-range order. Formation of different phases in Mo-Ru-B is dependent on boron content, but details of the structural inhomogeneity, that is, the distribution and spatial extent of these phases is probably more a function of quenching conditions. Such details could account for the observation of two superconducting transitions in one of our 18% boron samples. This sample, which is in the middle of the compositional range, could contain both types of short-range order with sufficient phase segregation to allow each region to possess a distinct transition temperature. Interestingly, the low T_c of the sample is the same as the T_c observed for the 22% boron sample. The behaviour of T_c is discussed further in the next section.

Similar behaviour in amorphous Ni-P and Zr-Cu alloys has recently been reported [53,54]. In the Ni-P system, NMR Knight shift measurements demonstrated the existence of two distinct local structural configurations at one composition. The configuration present was found to depend on the technique

used to produce the amorphous phase. The presence of two distinct superconducting transitions in melt-quenched ribbons of Zr-Cu alloys has been observed by Samwer. The composition of these alloys ranged from 26% Cu to 50% Cu; the samples used showed no evidence of crystallinity [55].

Although the exact nature of these short-range structural configurations-topology, spatial extent, etc.--cannot be determined by a bulk measurement such as specific heat, such a transition should be manifested in the density of states and transport properties such as the electrical resistivity ρ. Since resistivity primarily involves scattering events with momentum transfers of the order of twice the Fermi wavevector, it reflects changes in structure on the scale of interatomic distances [56].

Electrical conductivity in transition metals is usually viewed in terms of a two band model, whereby $\sigma = \sigma_s + \sigma_d$ [57,58]. But due to the large effective mass of the d electrons, most of the current is carried by the s electrons. A large contribution to the resistivity arises from scattering into unfilled d states near the Fermi level. The ratio of $s \rightarrow d$ scattering to $s \rightarrow s$ scattering roughly follows the relation [57].

$$\frac{\rho_{s \rightarrow d}}{\rho_{s \rightarrow s}} \sim \frac{N_d}{N_s}$$

where N_d and N_s are the d-band and s-band contributions to the density of states at ϵ_F. Evidence for this is shown by

the strong correlation between room temperature resistivity ρ and the electronic specific heat coefficient γ in the transition elements. Table 6 shows measured values of γ and ρ for transition elements of the 5B, 6B, 7B, and 8B periods. This correlation also follows from other factors, such as the variation of γ with electron effective mass, but clearly elements with high values of $N(\varepsilon_F)$ also exhibit high resistivities. The trend continues to the noble metals, in which ε_F lies above the filled d states.

This relationship contrasts with what we observe in amorphous Mo-Ru-B where the sharp decrease in $N(\varepsilon_F)$ is accompanied by an increase in resistivity. The reason may be that there is a significant contribution to conductivity from d electrons in these materials. The high value of the resistivity in these materials (on the order of 150 ohm-cm) is close to the "saturation" resistivity corresponding to the electron mean free path approaching the interatomic spacing [59]. This implies strong disorder scattering of the plane wave s electrons. Since d electron conduction most likely occurs by an intraband hopping mechanism among the extended d states of the solid [2], the d-band conduction could thus be of the same order as the s-band conduction. In this case, $N(\varepsilon_F)$ would influence the conductivity by determining the number of electrons involved in the conduction process. Hence, as in Mo-Ru-B, a structural change resulting in a decreased $N(\varepsilon_F)$ would be reflected in an increased electrical resistivity. Thus, the resistivity is tied to the

TABLE 6. Values of electronic specific heat coefficient γ in units of mJ mol^{-1} K^{-2} and room-temperature electrical resistivity ρ in μohm cm. (Taken from reference 7.)

	V	Cr	Mn	Fe	Co	Ni	Cu
γ	9.26	1.40	9.20	4.9	4.7	7.0	0.7
ρ	19.9	12.9	139	9.8	5.8	7.0	1.7
	Nb	Mo	Tc	Ru	Rh	Pd	Ag
γ	7.8	2.0	$\sim$7	3.3	4.9	9.4	0.65
ρ	14.5	5.3	$\sim$14	7.4	4.8	10.5	1.6
	Ta	W	Re	Os	Ir	Pt	Au
γ	5.9	1.3	2.3	2.4	3.1	6.8	0.73
ρ	13.1	5.3	18.6	9.1	5.1	10.4	2.2

behaviour of electrons in d states near the Fermi level.

In contrast to the Mo-Ru-B glasses, no discontinuities are evident in the composition dependence of the Mo-Ru-Si alloys. In Fig. 20, the bare (Fermi-level) density of states is plotted for both sets of alloys. The Si alloys show a smooth decrease with composition. Hence, we expect a small increase in resistivity with increasing Si content across the series. The measured resistivity of these alloys is essentially constant, but the relative error in the measurements is large [38]. A slight increase of ρ with Si content is not unreasonable in view of these uncertainties and this could be the source of the disagreement with γ values determined from $\frac{dH_{C2}}{dT}$ measurements.

As remarked earlier, the Debye temperature of the Mo-Ru-Si series increases with Si concentration and the value of θ_D=238K reported for amorphous $Mo_{58}Ru_{42}$ [48] is consistent with this trend. In addition, the observed Vicker's hardness for both Mo-Ru-B and Mo-Ru-Si alloys shows a roughly linear increase with metalloid content, with the effect being larger for Mo-Ru-B alloys [38] . Thus, one effect of addition of the light metalloids B and Si is to increase the Debye temperature of the amorphous phase. This is not surprising in view of the high values of the Debye temperature for these elements; 1220K for B and 630K for Si [3,7].

A comparison with elastic properties can be made for the Mo-Ru-B alloys since values of Young's modulus have been obtained for $(Mo_{.60}Ru_{.40})_{86}B_{14}$ and $(Mo_{.60}Ru_{.40})_{82}B_{18}$ alloys

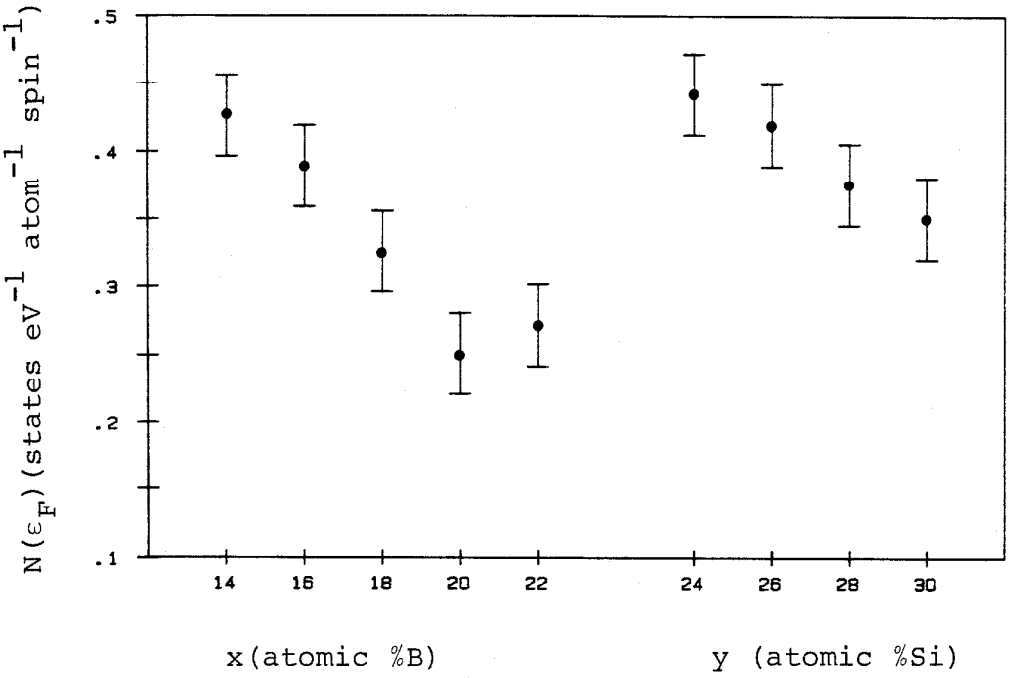

Figure 20. Density of states at the Fermi level in $(Mo_{.60}Ru_{.40})_{100-x}B_x$ alloys and in $(Mo_{.60}Ru_{.40})_{100-y}Si_y$ alloys calculated from $N(\varepsilon_F) = 3\gamma/[2\pi^2 k_B^2(1+\lambda)]$

[60]. These can be used to calculate Debye temperatures from the relation

$$\theta_D = 2.62 \frac{\hbar}{k_B} \left(\frac{E}{\rho}\right)^{1/2} \left(\frac{N}{V}\right)^{1/3}$$

We obtain the prefactor 2.62 by assuming a value for Poisson's ratio of 0.41. This is obtained from measured sound velocities of amorphous Pd and Pt alloys [61]. Using measured densities for these alloys [38], we calculate θ_D = 312K and 362K for $(Mo_{.60}Ru_{.40})_{86}B_{14}$ and $(Mo_{.60}Ru_{.40})_{82}B_{18}$, respectively. There are few such comparisons for metallic glasses but in general, it has been observed that the lattice specific heat of insulating glasses exceeds predictions based on elastic properties by a factor of 1-2 [27]. The values of θ_D that we have calculated indicate that the measured lattice specific heat is larger than predicted by factors of 1.2 and 2.0, respectively, for $(Mo_{.60}Ru_{.40})_{86}B_{14}$ and $(Mo_{.60}Ru_{.40})_{82}B_{18}$. Thus, although the calculated Debye temperatures depart considerably from the measured values, the magnitude of the departure agrees with general observations regarding the anomalous lattice specific heat of glasses.

B. Superconductivity

In this section, we examine the interplay between the parameters λ, $N(\varepsilon_F)$, and T_C in amorphous Mo-Ru-Si and Mo-Ru-B as evidenced by the specific heat data. It was shown by McMillan [15] that the electron-phonon coupling

constant could be considered as the product of an electronic part $\eta = N(\varepsilon_F)\langle I^2\rangle$ and a phonon part $\Phi = (M\langle\omega^2\rangle)^{-1}$. Attempts to systematize superconductivity in transition metals and alloys have generally focused on the behaviour of λ and of η, the so-called Hopfield parameter, since these strongly influence the transition temperature. The Hopfield parameter was originally viewed as being a constant across the transition series [15,62]. Hopfield [62] further argued that $N(\varepsilon_F)$ should have little influence on the transition temperature. However, calculations by Butler [63] show that a large part of the variation of λ across the 4d series is due to variations in $N(\varepsilon_F)$, particularly in the middle of the series. Recent work by Varma and others indicates that the factor $\langle I^2\rangle\Phi$ is constant and thus λ depends linearly on $N(\varepsilon_F)$ [64,65].

For the Mo-Ru-Si alloys, an increase in the Debye temperature with increasing silicon content is accompanied by a decrease in T_c. This indicates an overall decrease in the strength of the electron-phonon coupling, as shown by values of λ computed with the McMillan expression. In the Mo-Ru-B series, λ appears to be approximately constant across most of the series but decreases for the 22% boron sample, which had a particularly low T_c. When λ values for all alloys are plotted as a function of metalloid content as in Fig. 21, it appears that λ decreases in a roughly linear fashion and is more dependent on the number of metalloid atoms present than on the type of atom. Linearly extrapolating

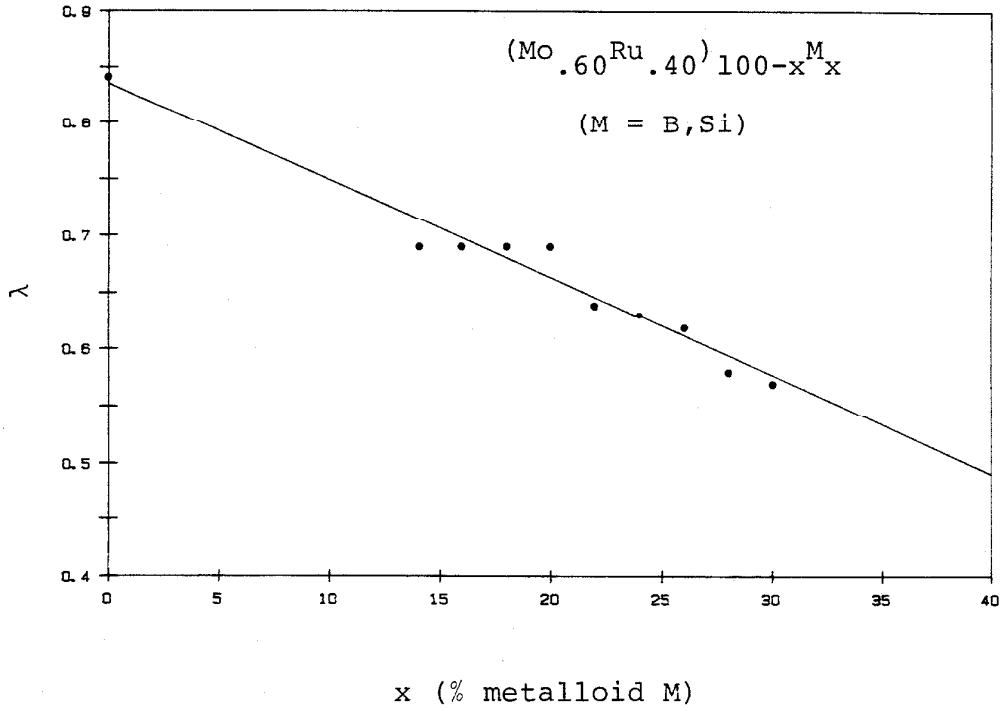

Figure 21. Electron phonon coupling constant plotted as a function of metalloid content.

the values of λ to x = 0 (corresponding to a composition $Mo_{60}Ru_{40}$) yields a value of $\overline{\lambda}$ = 0.83, which is close to the value of λ = 0.84 computed for amorphous $Mo_{58}Ru_{42}$ [48]. This linear relationship suggests a dilution of the d-band due to the decreased density of transition metal atoms [38]. However, since $\langle\omega^2\rangle \sim \theta_D^2$, the observation that θ_D increases with increased B and Si content implies that addition of metalloids acts to increase the averaged squared phonon frequency $\langle\omega^2\rangle$. This in turn would decrease λ, since $\lambda \sim 1/\langle\omega^2\rangle$.

The electron-phonon coupling constant λ appears to be more strongly influenced by the electronic structure. Based on non-orthogonal tight binding calculations, Varma and Dynes predict that

$$\delta = \frac{\lambda}{N(\varepsilon_F)} = W(1 \mp S)$$

should be a constant for a class of materials dominated by the same type of orbital near the Fermi surface [64]. In this expression, W is related to the width of the d-band and S is the overlap integral of orbitals on neighboring sites. The + sign refers to ε_F in the upper or antibonding half of the d-band while the - sign is for ε_F in the lower or bonding half of the band. Generally, the density of states curve of crystalline transition metals can be described as having two peaks separated by a region of low density. In bcc alloys, these two peaks correspond to the bonding and antibonding d orbitals near the Fermi level [2]. This two-peaked structure

is mirrored in the Matthias rules for the superconductivity of transition metals [66]. Plotting T_C versus electron-to-atom ratio for the 4d series as in Fig. 22, it is evident that high T_C phases occur for e/a values near 4.5 and 6.5. Also shown in Fig. 22 is the Collver-Hammond [67] curve which, in a similar fashion, is thought to reflect the density of states of amorphous transition metals. The two peak behaviour of the crystalline T_C curve appears to be broadened into a rather featureless single peak for the amorphous materials. Nonetheless, the Varma-Dynes model is reasonably successful in accounting for the behaviour of amorphous transition metal superconductors. Johnson and Tenhover [68] have shown that for both crystalline and amorphous alloys of Zr, Nb, and Mo, λ versus $N(\varepsilon_F)$ data could be grouped on two well defined lines. These were interpreted as resulting from the positioning of the Fermi level (either in the upper or lower half of the band) in accordance with the Varma-Dynes relationship. This grouping corresponded with Fermi level positions that would be expected from the electron-to-atom ratio in the different alloys.

The lines obtained by Johnson and Tenhover are reproduced in Fig. 23 along with data for the Mo-Ru-B, Mo-Ru-Si, and $Mo_{58}Ru_{42}$ alloys. Since e/a is approximately 6.8 for $Mo_{60}Ru_{40}$ we expect ε_F to be in the upper part of the d-band, corresponding to the upper curve in the figure. As shown, the data for all Mo-Ru-Si alloys, $Mo_{58}Ru_{42}$ and $(Mo_{.60}Ru_{.40})_{86}B_{14}$ and $(Mo_{.60}Ru_{.40})_{84}B_{16}$ lie on or near the upper curve. For Mo-Ru-B

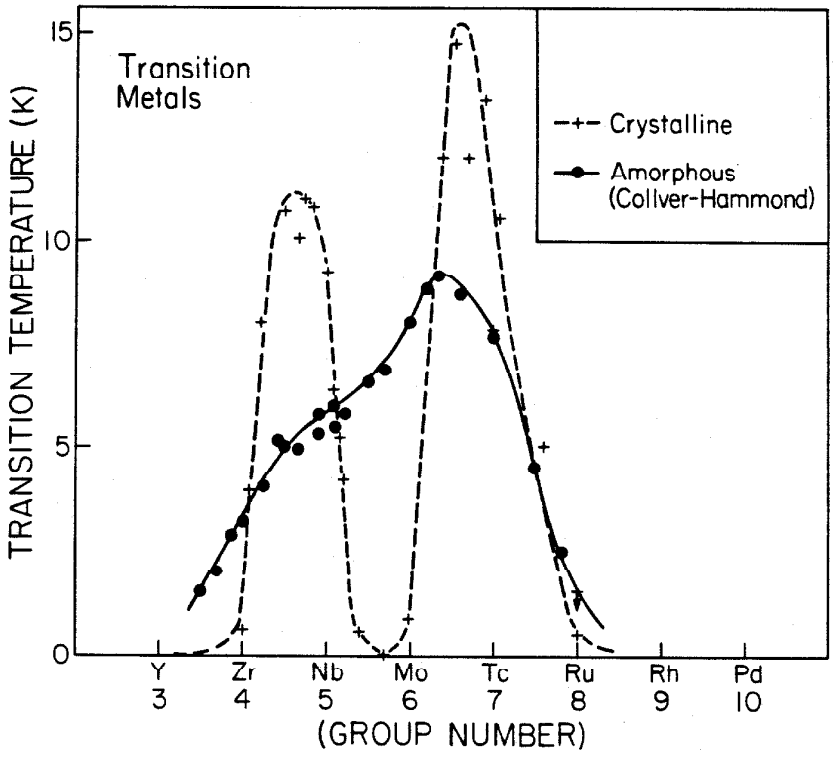

Figure 22. Transition temperature versus electron-to-atom ratio (average group number) for crystalline and amorphous 4d transition metals and alloys. (Taken from reference 43.)

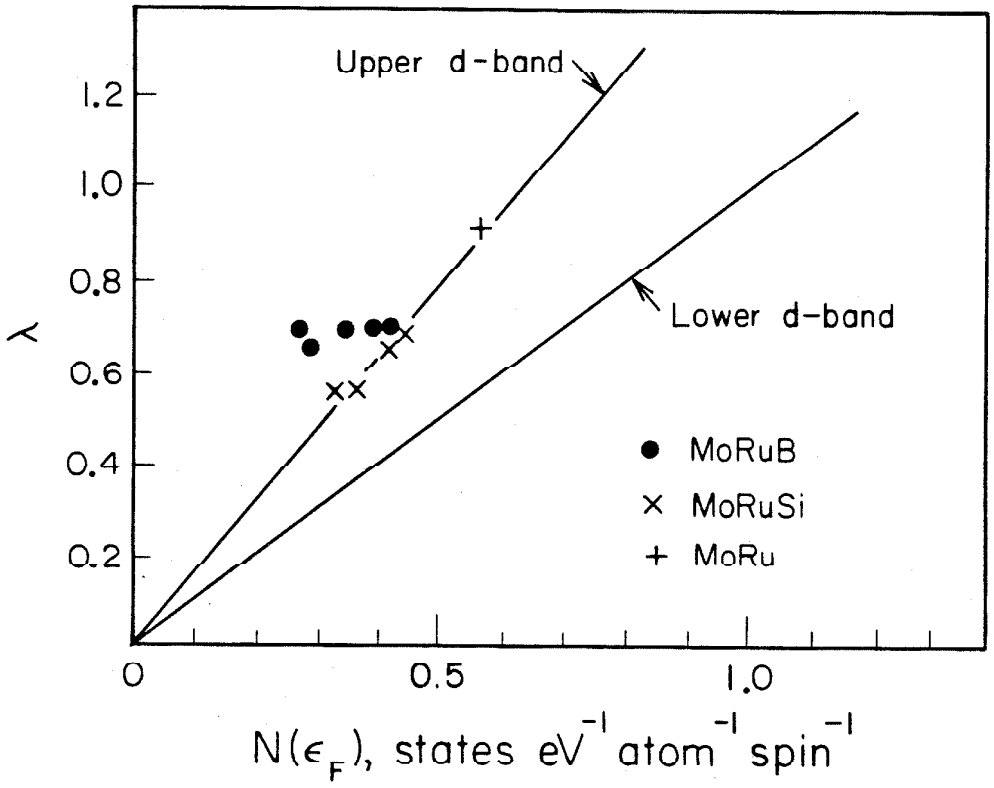

Figure 23. Electron phonon coupling constant plotted against density of states at the Fermi level for amorphous Mo-Ru-B, Mo-Ru-Si, and Mo-Ru alloys. Solid lines represent results given in reference 68.

alloys with $x \geq 18\%$ B, the data points deviate from the Varma-Dynes curve as $N(\varepsilon_F)$ decreases.

If the high boron phase of Mo-Ru-B which we have identified as having a low γ is a well defined single-phase material, then the Varma-Dynes concept should still apply. This suggests that the d bandwidth W_d is increased for the high boron phase which in turn may be the cause of the observed decrease in the density of states. How this is reflected in resistivity is not clear, since ρ depends on both $N(\varepsilon_F)$ and W_d. In tight binding theory, the width of the d-band is a function of the average short-range order near a transition atom [2]. It is related to an average of matrix elements of the form

$$\beta = \langle i,m|V_j|j,m' \rangle$$

where $|i,m\rangle$ is an atomic d level on site i with orbital moment m; V_j is an atomic potential centered on lattice site j. Such matrix elements mix the atomic d levels into extended states of the solid. Thus, the atomic d states are broadened into a band of width W_d. The mean lifetime τ of an electron in these states is of the order of h/W_d giving an interatomic hopping frequency of $1/\tau$. The conductivity associated with such a mechanism should therefore increase as the bandwidth increases. If we are to assume a high degree of d-band conduction, then this effect must be smaller than the effect of a decreasing density of states.

The transition temperature in these systems depends on the electron-phonon coupling primarily through the behaviour

of $N(\varepsilon_F)$. In Figs. 24 and 25, we plot T_c as a function of λ and of $N(\varepsilon_F)$. (Results for the $(Mo_{.60}Ru_{.40})_{82}B_{18}$ sample which showed two transitions are not included.) The dependence of T_c on λ is not surprising since λ is calculated using the same measured values of T_c. However, these is a correlation between T_c and $N(\varepsilon_F)$ for each alloy series. This correlation also exists for the higher T_c Mo-Ru phases, both crystalline and non-crystalline. The dependence arises through the influence of $N(\varepsilon_F)$ on λ, but it is apparent that details of the atomic arrangements do not strongly influence T_c. We have argued that $N(\varepsilon_F)$ should depend to a large extent on the local environment of the metal atoms, and T_c clearly depends on $N(\varepsilon_F)$. However, the transition temperature does not exhibit the discontinuous behaviour observed for other properties of the Mo-Ru-B system near 18% boron [38]. Evidently, in these systems, superconductivity is not as sensitive to changes in short-range order. This is a consequence of the characteristic length scale for superconductivity being larger than that for structural inhomogeneities in these materials [69]. The superconducting coherence length, which gives roughly the spatial overlap of the paired electrons, is estimated to be on the order of 100 Å [70]. This gives a natural length for changes in the superconducting properties. Thus, the structural changes which occur on the scale of a few atomic diameters that can be reflected in, for example, the electrical resistivity, may not be reflected in superconductivity.

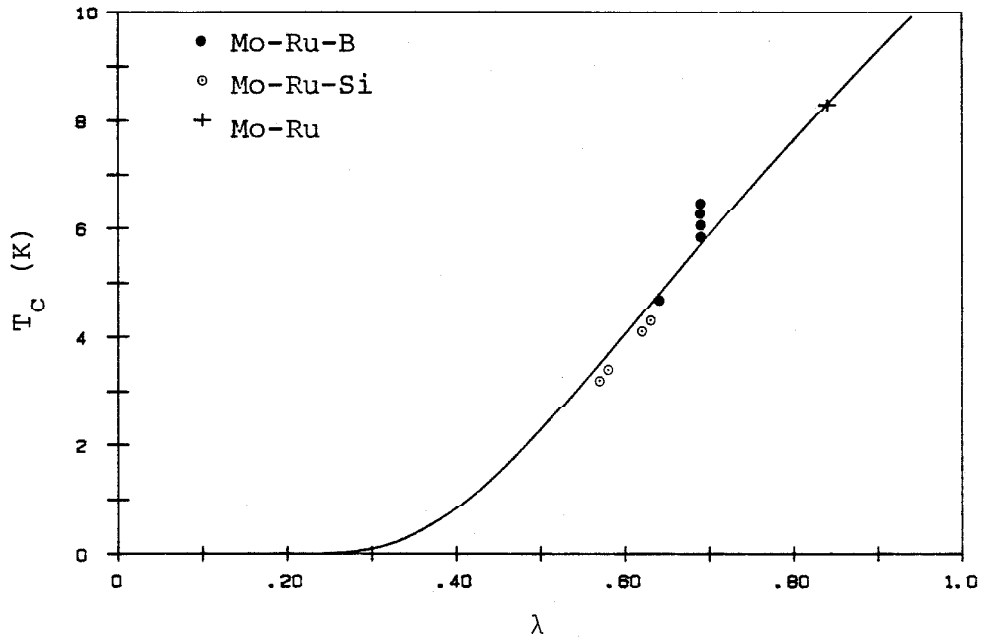

Figure 24. Transition temperature T_c plotted as a function of the electron-phonon coupling constant λ for amorphous alloys. Solid line shows the relationship $T_c \sim e^{-1/(\lambda - \mu^*)}$.

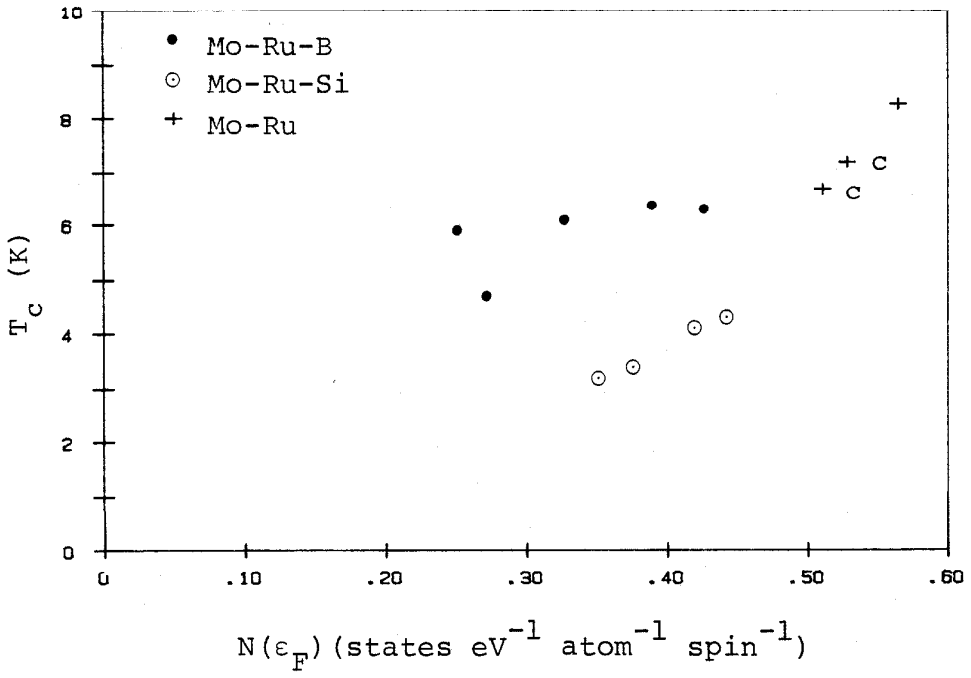

Figure 25. Transition temperature T_c plotted as a function of the density of states at the Fermi level $N(\varepsilon_F)$. ("c" denotes a crystalline alloy.)

V. SUMMARY

V. SUMMARY

In this thesis, low temperature specific heat data for transition metal-metalloid glasses of molybdenum and ruthenium alloyed with boron and silicon have been reported. The data were obtained from measurements which employed a thermal relaxation time technique developed for small samples.

There is strong evidence for the presence of two distinct amorphous phases in Mo-Ru-B alloys, characterized by different local structures. By contrast, the structure of Mo-Ru-Si alloys seems to be dominated by a single type of short-range order. However, the idea of structural inhomogeneities in metallic glasses must be viewed in terms of the length scales involved, as this determines to what extent macroscopic properties are sensitive to variations in local atomic arrangements. The properties of Mo-Ru-B and Mo-Ru-Si glasses which we have considered in detail are the normal state electrical resistivity and superconductivity. We have attempted to demonstrate the strong influence of the density of states at the Fermi level $N(\varepsilon_F)$ on these properties. In Mo-Ru-B, the increase in the resistivity with increasing boron content has been related to the decrease in $N(\varepsilon_F)$. This implies a conduction mechanism in these materials in which a substantial part of the current is carried by d electrons. This contrasts with the case of crystalline transition metals, where changes in resistivity are associated with similar changes in $N(\varepsilon_F)$. The applicability of the Varma-Dynes model to the superconductivity of Mo-Ru-Si and an amorphous Mo-Ru alloy is

indicated by the linear dependence of the electron-phonon coupling constant λ on $N(\varepsilon_F)$. These phases appear to be closely related. The deviation from the Varma-Dynes picture exhibited by Mo-Ru-B alloys with high boron content may follow from the structural change which is manifested in resistivity and density of states.

Alloying with metalloids B and Si increases the Debye temperature of the amorphous Mo-Ru phase and can be correlated with an overall depression of λ. The latter effect may follow directly from the influence of B and Si on the average phonon frequencies or indirectly from the effect metalloid atoms have on the d-band density of states. For two of the Mo-Ru-B alloys, calculations of the Debye temperature from measured elastic properties show that these materials exhibit the excess lattice specific heat observed in many insulating glasses.

REFERENCES

1. P. Duwez, in Glassy Metals I (Topics in Applied Physics, v. 46), H.-J. Güntherodt and H. Beck, ed., Springer-Verlag, Berlin, 1981; and W. Klement, Jr., R. H. Willens and P. Duwez, Nature 187, 869 (1960).

2. J. Friedel, in The Physics of Metals, v.1, Electrons, J. M. Ziman, ed., Cambridge University Press, Cambridge, 1969.

3. E. S. R. Gopal, Specific Heats at Low Temperatures, Plenum Press, New York, 1966.

4. General references used for section II.1 are:
(a) N. W. Ashcroft and N. D. Mermin, Solid State Physics, Holt, Rinehart and Winston, New York, 1976; and
(b) F. Reif, Fundamentals of Statistical and Thermal Physics, McGraw-Hill, New York, 1965.

5. T. H. K. Barron and J. A. Morrison, Can. J. Phys. 35, 799 (1957).

6. See reference 4(a), ch. 22.

7. C. Kittel, Introduction to Solid State Physics, 5th ed., John Wiley and Sons, New York, 1976.

8. (a) W. A. Harrison, Solid State Theory, Dover Publications, New York, 1979; (b) W. A. Harrison, Electronic Structure and the Properties of Solids, W. H. Freeman and Company, San Francisco, 1980.

9. M. Tinkham, Introduction to Superconductivity, McGraw-Hill, New York, 1975.

10. D. Saint-James, G. Sarma and E. J. Thomas, Type II

Superconductivity, Pergamon Press, Oxford, 1969.

11. J. Bardeen, L. N. Cooper, and J. R. Schrieffer, Phys. Rev. 108, 1175 (1957).
12. G. Rickayzen, in Superconductivity, v.1, R. D. Parks, ed., Marcel Dekker, New York, 1969.
13. B. Mühlschlegel, Z. Phys. 155, 313 (1959).
14. M. Abramowitz and I. A. Stegun, Handbook of Mathematical Functions, National Bureau of Standards, Washington, 10th Printing, 1972, p. 358.
15. W. L. McMillan, Phys. Rev. 167, 331 (1968).
16. G. M. Eliashberg, Soviet Phys. JETP 11, 696 (1960).
17. P. B. Allen and R. C. Dynes, Phys. Rev. B 12, 905 (1975).
18. T. P. Orlando, E. J. McNiff, Jr., S. Foner and M. R. Beasley, Phys. Rev. B 19, 4545 (1979).
19. P. Chaudhari and D. Turnbull, Science 199, 11 (1978).
20. D. E. Polk and B. C. Giessen, in Metallic Glasses, American Society for Metals, 1976.
21. P. Pietrokowsky, Rev. Sci. Instr. 34, 445 (1963).
22. H. S. Chen and C. E. Miller, Met. Res. Bull. 11, 49 (1976).
23. A. R. Williams, Ph.D. Thesis, California Institute of Technology, Pasadena, California, 1981.
24. G. S. Cargill III, Solid State Physics 30, 227 (1975).
25. W. A. Phillips, ed., Amorphous Solids: Low Temperature Properties, Springer-Verlag, Berlin, 1981.
26. P. W. Anderson, B. I. Halperin and C. M. Varma, Phil. Mag. 25, 1 (1972); and W. A. Phillips, J. Low Temp. Phys. 7, 351 (1972).

27. R. O. Pohl, in reference 25.

28. R. Dachmann, F. J. DiSalvo, Jr., T. H. Geballe, R. L. Greene, R. E. Howard, C. N. King, H. C. Kirsch, K. N. Lee, R. E. Schwall, H.-U. Thomas and R. B. Zubeck, Rev. Sci. Instr. 43, 205 (1972).

29. W. H. Shull, D. G. Naugle, S. J. Poon and W. L. Johnson, Phys. Rev. B 18, 3263 (1978).

30. Lake Shore SCS-1 manufactured by Lake Shore Cryotronics, 64 E. Walnut St., Westerville, Ohio 43081.

31. Manufactured by Wakefield Engineering, Wakefield, Mass. 01880.

32. D. L. Martin, Phys. Rev. B 8, 5357 (1973) and references therein.

33. Manufactured by Apiezon Products Ltd., 4 York Road, London S.E. 1.

34. N. E. Phillips, Phys. Rev. 114, 676 (1959); J. L. Cude and L. Finegold, Cryogenics 11, 394 (1971); M. Wun and N. E. Phillips, Cryogenics 15, 36 (1975); and R. D. Shull, private communication.

35. See reference 14, p. 228.

36. Manufactured by General Electric Company, Insulating Materials Dept., Schenectady, New York, 12305.

37. A brief account of this work is given in S. T. Hopkins and W. L. Johnson, Solid State Comm. 43, 537 (1982).

38. W. L. Johnson and A. R. Williams, Phys. Rev. B 20, 1640 (1979).

39. S. T. Hopkins, unpublished.

40. U. Mizutani and T. B. Massalski, J. Phys. F 10, 1093 (1980).

41. M. Tenhover, unpublished.

42. The area under the Mössbauer spectra is related to a Debye-Waller factor which can be modelled using a Debye phonon spectrum. See, for example, C. Kittel, Quantum Theory of Solids, John Wiley and Sons, New York, 1963.

43. W. L. Johnson, in Glassy Metals I (Topics in Applied Physics, v.46), H.-J. Güntherodt and H. Beck, ed., Springer-Verlag, Berlin, 1981.

44. M. Tenhover, private communication.

45. E. R. Domb, C. A. MacDonald and W. L. Johnson, Solid State Comm. 30, 775 (1979).

46. E. Bucher, F. Heiniger and J. Müller, Phys. Kondens. Materie 2, 210 (1964).

47. F. J. Morin and J. P. Maita, Phys. Rev. 129, 1115 (1963).

48. S. R. Early, F. Hellman, J. Marshall and T. H. Geballe, Physica 107B, 327 (1981).

49. F. Heiniger, E. Bucher and J. Müller, Phys. Kondens. Materie 5, 243 (1966).

50. L. F. Mattheiss, in Superconductivity in d- and f-Band Metals, D. H. Douglass, ed., American Institute of Physics, New York, 1972.

51. N. F. Mott and E. A. Davis, Electronic Processes in Non-Crystalline Materials, 2nd ed., Clarendon Press, Oxford, 1979, ch. 2.

52. F. A. Cotton and G. Wilkinson, Advanced Inorganic

Chemistry, 3rd ed., John Wiley and Sons, New York, 1972.

53. D. S. Lashmore, L. H. Bennett, H. E. Schone, P. Gustafson and R. E. Watson, Phys. Rev. Lett. 48, 1760 (1982).

54. K. Samwer and H. v. Löhneysen, Phys. Rev. B 26, 107 (1982).

55. K. Samwer, private communication.

56. W. L. Johnson, in Metastable Materials Formation by Ion Implantation, S. T. Picraux and W. J. Choyke, ed., Elsevier Science Publishing, 1982.

57. J. M. Ziman, Electrons and Phonons, Clarendon Press, Oxford, 1960.

58. N. F. Mott and H. Jones, The Theory of the Properties of Metals and Alloys, Dover, New York, 1958.

59. P. J. Cote and L. V. Meisel, in Glassy Metals I (Topics in Applied Physics, v.46), H.-J. Güntherodt and H. Beck, ed., Springer-Verlag, Berlin, 1981.

60. C. Silvestre, Senior Thesis, California Institute of Technology, Pasadena, Califoria, 1980.

61. L. A. Davis, in Rapidly Quenched Metals (Proceedings of Second International Conference on Rapidly-Quenched Metals), N. J. Grant and B. C. Giessen, ed., MIT Press, 1976.

62. J. J. Hopfield, Phys. Rev. 186, 443 (1969).

63. W. H. Butler, Phys. Rev. B 15, 5267 (1977).

64. C. M. Varma and R. C. Dynes, in Superconductivity in d- and f-band Metals, D. H. Douglass, ed., Plenum, New York, 1976.

65. C. M. Varma and W. Weber, Phys. Rev. B 19, 6142 (1979).

66. B. T. Matthias, Prog. Low. Temp. Phys. 2, 138 (1957).

67. M. M. Collver and R. H. Hammond, Phys. Rev. Lett. 30, 92 (1973).

68. W. L. Johnson and M. Tenhover, in The Magnetic, Chemical and Structural Properties of Glassy Metallic Alloys, R. Hasegawa, ed., CRC Press, 1982.

69. W. L. Johnson, to appear in Superconductivity in d- and f-band Metals, W. Buckel, ed., 1982.

70. B. M. Clemens, W. L. Johnson, and J. Bennett, J. Appl. Phys. 51, 1116 (1980).